



HAL
open science

Climatology of aerosol properties and clear-sky shortwave radiative effects using Lidar and Sun photometer observations in the Dakar site

A. Mortier, P. Goloub, Y. Derimian, D. Tanré, T. Podvin, L. Blarel, C. Deroo,
B. Marticorena, A. Diallo, T. Ndiaye

► To cite this version:

A. Mortier, P. Goloub, Y. Derimian, D. Tanré, T. Podvin, et al.. Climatology of aerosol properties and clear-sky shortwave radiative effects using Lidar and Sun photometer observations in the Dakar site. Journal of Geophysical Research: Atmospheres, 2016, 121, pp.6489-6510. 10.1002/2015JD024588 . insu-03686205

HAL Id: insu-03686205

<https://insu.hal.science/insu-03686205>

Submitted on 2 Jun 2022

HAL is a multi-disciplinary open access archive for the deposit and dissemination of scientific research documents, whether they are published or not. The documents may come from teaching and research institutions in France or abroad, or from public or private research centers.

L'archive ouverte pluridisciplinaire **HAL**, est destinée au dépôt et à la diffusion de documents scientifiques de niveau recherche, publiés ou non, émanant des établissements d'enseignement et de recherche français ou étrangers, des laboratoires publics ou privés.



Distributed under a Creative Commons Attribution - NonCommercial - ShareAlike 4.0 International License



RESEARCH ARTICLE

10.1002/2015JD024588

Key Points:

- Characterization of aerosols with remote sensing and in situ measurements over different time scales
- Climatology of aerosol vertical profiles
- Radiative effect and heating rate calculation

Supporting Information:

- Supporting Information S1

Correspondence to:

A. Mortier,
augustinmortier@gmail.com

Citation:

Mortier, A., P. Goloub, Y. Derimian, D. Tanré, T. Podvin, L. Blarel, C. Deroo, B. Marticorena, A. Diallo, and T. Ndiaye (2016), Climatology of aerosol properties and clear-sky shortwave radiative effects using Lidar and Sun photometer observations in the Dakar site, *J. Geophys. Res. Atmos.*, 121, 6489–6510, doi:10.1002/2015JD024588.

Received 2 DEC 2015

Accepted 13 MAY 2016

Accepted article online 19 MAY 2016

Published online 11 JUN 2016

Climatology of aerosol properties and clear-sky shortwave radiative effects using Lidar and Sun photometer observations in the Dakar site

A. Mortier^{1,2}, P. Goloub¹, Y. Derimian¹, D. Tanré¹, T. Podvin¹, L. Blarel¹, C. Deroo¹, B. Marticorena³, A. Diallo⁴, and T. Ndiaye⁴

¹Laboratoire d'Optique Atmosphérique, CNRS-Université de Lille 1, Villeneuve d'Ascq, France, ²Now at MetNo, Oslo, Norway, ³Laboratoire Inter-universitaire des Systèmes Atmosphériques, CNRS-Université de Paris 7–12, Créteil, France,

⁴Institut de Recherche pour le Développement, Dakar, Sénégal

Abstract This paper presents the analysis of nearly a decade of continuous aerosol observations performed at the Mbour site (Senegal) with Sun photometer, Lidar, and Tapered Electromagnetic Oscillating Microbalance. This site is influenced all year-round by desert dust and sporadically, in wintertime, by biomass burning particles. Different patterns are revealed for winter and summer, seasons associated to air masses of different origin. The summer (wet season) is characterized by a high aerosol loading (optical thickness, AOT, around 0.57 at 532 nm) composed of large and weakly absorbing particles (Angstrom exponent, α , of 0.23 and single-scattering albedo, ω_0 , of 0.94 at 532 nm). A lower aerosol loading (AOT = 0.32) is observed during winter (dry season) for finer and absorbing particles ($\alpha = 0.48$ and $\omega_0 = 0.87$) revealing the presence of biomass burning aerosols and a greater proportion of local emissions. This latter anthropogenic contribution is visible at weekly and daily scales through AOT cycles. A decrease of about 30% in AOT has been featured in autumn since 2003. The derivation of the extinction profiles highlights a dust transport close to the ground during winter and in an aloft layer (up to 5 km) during summer. Accurate calculations of the daily aerosol radiative effect in clear-sky conditions are finally addressed. From spring to winter, seasonal shortwave radiative forcing averages of 14.15, 11.15, 8.92, and 12.06 W m⁻² have been found respectively. Up to 38% of the solar clear-sky atmospheric heating can be attributed to the aerosols in this site.

1. Introduction

With the largest worldwide dust emissions coming from extensive deserts such as Sahara and Sahel, Africa plays a major role in the aerosols global emission [Prospero *et al.*, 2002] reinforced, sporadically, with important emissions of biomass burning aerosols [Delmas *et al.*, 1991; Pelon *et al.*, 2008]. Due to their different optical and microphysical properties, these particles interact differently with the electromagnetic radiations. The dust particles are mainly acting through the direct effect, while the smaller but absorbing biomass burning particles are also involved in the semidirect effect [Sathesh and Krishnamoorthy, 2005]. Although the number of studies focusing on the aerosol radiative effect over Africa increased these last years, a large uncertainty remains regarding the radiative impact of the aerosols over this area [Haywood *et al.*, 2003; Tanré *et al.*, 2003]. One of the reasons is the high variability of the particles in space and time whose better understanding requires comprehensive observations of the aerosols in their natural environment. Spaceborne instruments, passive such as MODIS (Moderate Resolution Imaging Spectroradiometer) or active ones as Cloud-Aerosol Lidar with Orthogonal Polarization deliver useful multiyear observation databases covering large domains. Nevertheless, the information is not continuous in time and limited by the constraining observation conditions. Some measurements are performed from the ground through different campaigns [Haywood *et al.*, 2008; Heintzenberg, 2009] but are usually limited to short time periods.

In 1996, the LOA (Laboratoire d'Optique Atmosphérique), in cooperation with the IRD (Institut de Recherche pour le Développement), started to conduct continuous Sun photometer observations in the Mbour site, also referred as the Dakar site, in Senegal, West Africa. These observations were completed 10 years later with the setup of a Lidar and in situ instruments that perform continuous measurements ever since. West Africa is an intricate study region since the related aerosols are complex mixtures of biomass burning aerosols, desert dust, and anthropogenic emissions from traffic or domestic fires [Flament *et al.*, 2011; Liousse *et al.*, 2010]. In addition, the proximity of the site to the Atlantic Ocean implies an oceanic influence. The composition

©2016. The Authors.

This is an open access article under the terms of the Creative Commons Attribution-NonCommercial-NoDerivs License, which permits use and distribution in any medium, provided the original work is properly cited, the use is non-commercial and no modifications or adaptations are made.

of the particles observed over this site depends on the atmospheric circulation which is mainly driven, at this latitude (14.4°N), by the annual ITCZ (Intertropical Convergence Zone) oscillation [Gyoswami and Shukla, 1984] responsible for two contrasted seasons: the dry and the wet seasons. During summer, the desert-dust particles are transported westward toward the Atlantic Ocean in elevated layers and can be observed over Canary Islands [Bergametti *et al.*, 1989; González and Urós, 2011] or Capo Verde [Ansmann *et al.*, 2009; Gama *et al.*, 2015]. In contrast, during winter, the dust particles are rather transported close to the ground [Chiapello *et al.*, 1995].

Three years of observations (2006–2008) performed over this site have been presented by Léon *et al.* [2009]. The height variations of the dust transport have been investigated thanks to the Lidar vertical profiles. Even though seasonal patterns could be noticed, the data set could not allow the exploration of the interannual variability as well as the multiannual trends. At present time, thanks to a maintained effort at the instrumentation level, the database is substantial enough to achieve these goals. New robust and automatic algorithms have been developed and applied in order to process quality-checked retrievals over a large database.

The main objectives of this work are as follows: (i) to study seasonal and interannual variability of aerosol properties by combining a large database of sunphotometric retrievals, namely, optical and microphysical properties, with Lidar data, such as extinction profiles and layer heights, over a long time period and (ii) to benefit from the simultaneously obtained total column photometric and vertically resolved Lidar observations in order to better assess the aerosol direct radiative effect.

The paper is structured as the following: the instrumentation and the methodology used in this work are presented in section 2. In section 3, we focus on the variability of the aerosol characteristics, from column-integrated properties to vertical distribution. After describing the variation of the different parameters, we propose an interpretation of the trends observed over different time scales while taking into account the air masses trajectories and the weather records. Finally, in the last section, we calculate the aerosol radiative effect in the Dakar site while benefitting from knowledge of the aerosol vertical profiles and highlighting its important contribution.

2. Instruments and Methodology

The Mbour observation platform is located on the roof of the IRD center, 80 km south of Dakar. This site is located near the Atlantic Ocean, at less than 100 m from the seashore. It belongs to a nature reserve and is therefore relatively distant from direct urban particle emissions. The observations of aerosol properties are performed by means of both remote sensing (passive and active) and in situ instruments.

2.1. Sun Photometer

The Sun photometer measurements have been conducted since December 1996 with CE-318 Cimel Sun photometers integrated into Aerosol Robotic Network (AERONET) [Holben *et al.*, 1998]. Sporadic in time during the earlier years, the observations became continuous in May 2003. The standard CE-318 Sun photometers automatically measure the atmospheric transmission and the sky radiance at several scattering angles. These measurements are collected at several wavelengths, from UV to the near-infrared spectral domain, using nine filters passing sequentially in front of the detector. These filters have a bandwidth of about 10 nm, which is respectively centered in 340, 380, 440, 500, 670, 870, 936, 1020, and 1640 nm.

The direct measurements lead to the aerosol optical thickness (AOT) which is an extensive parameter mostly driven by the amount of particles and to the Angstrom exponent (α), derived from a couple of spectral AOT, which vary with the particles size. The accuracy of the AOT depends on the wavelength. It is expected to be lower than 0.01 for a wavelength, denoted λ , greater than 400 nm and lower than 0.02 elsewhere [Holben *et al.*, 1998]. Inversion of the radiation field measurements provides information on the microphysical properties of the observed aerosol [Dubovik and King, 2000]. That is, the volume size distribution (VSD) and, when the AOT level enables ($\text{AOT} \geq 0.4$ at 440 nm), the complex refractive index (RI), decomposed as $m = m_r - i m_i$ where m_r and m_i are, respectively, the real and the imaginary part), and therefore the single-scattering albedo (hereafter written ω_0). An estimation of the expected accuracy for these parameters can be found in Dubovik *et al.* [2000]. Fraction of spherical/nonsphericity particles is also retrieved [Dubovik *et al.*, 2002]. These different retrievals are provided by the AERONET data processing, which ensures as well the cloud screening for data levels 1.5 and 2.0 [Smirnov *et al.*, 2000]. For this reason, only these data levels are used in this work.

All the parameters delivered from the photometric observation are integrated for the entire atmospheric column; the vertical distribution of the aerosol, however, can be investigated thanks to active remote sensing instruments.

2.2. Lidar

In the context of the African Monsoon Multidisciplinary Analyses campaign (2006), the aerosol observation has been reinforced on the site with the setting up of a monoaxial Cimel Micro-Pulsed Lidar (CAML CE-370). The main advantage of this simple Lidar lies in its robustness and in its capability of automatic and continuous running in extreme conditions, which is required for studying the variability in the aerosol characteristics over different time scales. The Lidar provides attenuated backscatter profiles at 532 nm up to a height of 30 km, with a vertical resolution of 15 m. A description of the CAML CE-370 instrument characteristics can be found in more details in the literature [Pelon *et al.*, 2008]. The raw signal is corrected from the nonlinearity of the avalanche photodiode detectors, from the background radiation and with the overlap function. The latter was calculated with horizontal measurements and is regularly checked during clear atmospheric conditions by comparing the profiles with a simulated theoretical Rayleigh profile. Due to the afterpulse phenomenon, which results from a stray light due to internal reflections during the emission phase, the first 250 m cannot be used.

The extinction profiles, σ_{ext} , are calculated with 15 min averaged backscatter profiles thanks to the Klett-Fernald method [Klett, 1981, 1985] constrained by the AOT measured by the colocated Sun photometer. For this kind of device, the expected accuracy on the retrievals has been discussed in Mortier [2013]. A constant extrapolation is performed on the extinction profile for the first 250 m during the inversion procedure, in order to minimize the bias that would be induced with an incomplete vertical profile. The Lidar retrievals used in this study are the extinction profile and an associated Lidar Ratio, denoted S_a and also called extinction to backscatter ratio, whose constant value along the profile, due to the lack of information, is an indicator of the dominating type of aerosols observed in the column. In order to improve the signal-to-noise ratio, a Gaussian bandwidth filter is applied to the fast Fourier transform of the signal. Thus, 50% of the highest frequencies that are mainly responsible of the instrumental noise are reduced.

Cloud detection, based on the vertical variability of the signal [Pal *et al.*, 1992], was developed in order to consider aerosol profiles only. Some thresholds are involved in the detection process, but these take into account the noise level of the signal, providing a robust detection. Thus, by using constant thresholds over the whole database, a good discrimination of aerosols and clouds has been observed for very contrasted scenes and even considering a time-evolving instrumentation. A description of the cloud-detection method can be found in more details in Mortier *et al.* [2013]. Remaining clouds in Lidar profiles or Sun photometer measurements would lead, in most of cases, to nonphysical S_a values. A minimum and a maximum boundary were chosen, as respectively, 5 sr and 120 sr, for eliminating such possible residual contamination, as well as some instrumental issues. Finally, profiles with negative extinction values below a height of 3 km were excluded. Such cases can be observed if a wrong overlap function is applied.

Two different layer heights are detected, when possible, in every profile. The first is the planetary boundary layer, or PBL, which refers to the strongest vertical gradient. The second one is the top layer (TL), which refers, as introduced by Léon *et al.* [2009], to the top of the aloft aerosol layer if the vertical gradient is significant enough. The vertical variability of the profiles is studied thanks to the wavelet technic [Baars *et al.*, 2008; Brooks, 2003]. A detailed description of the method is presented by Mortier [2013]. One can note that the automatic processing of Lidar data algorithm (BASIC) is distributed (open source) by the ICARE data center that uses it for computing the observations of various Lidars integrated into the French Network (Observations en Réseaux des Aérosols à Usage de Recherches Environnementales (ORAURE)).

2.3. TEOM

A commercial TEOM 1400A (Tapered Electromagnetic Oscillating Microbalance) from Thermo Scientific Company, maintained by the Laboratoire Inter-universitaire des Systèmes Atmosphériques, has been operating on the observation site since 2006. The instrument characteristics and the measurement procedure are described in Marticorena *et al.* [2010]. In brief, the principle is the study of the vibration frequency shift of an oscillating conic element. This change of frequency is then linked to the mass concentration of the surrounding air aspirated through a vertical chimney. A size-selecting filter placed within the chimney allows the PM_{10} measurement, which refers to the mass concentration of particles whose aerodynamic diameter

is below 10 μm . One should notice that the measurement process includes a heating of the aspired air to about 50°C in order to ensure the thermic stability of the system and to avoid the condensation. Nevertheless, this heating can imply the loss of volatile organic compounds, as well as marine aerosols that might be present on the site, depending on the wind direction. The hourly measurements, which are the finest time resolution measurements available, are used in this work.

2.4. Weather Station

In addition, a standard weather station operates on the observation platform. It provides measurements of temperature, pressure, relative humidity (RH), wind speed, and wind direction. The measurements are available since 2006 with a time period of 6 h.

3. Variability of Aerosol Properties

3.1. Meteorological Context

Due to its geographical location (14.39°N, 19.9°W), Mbour is under influence of the Intertropical Convergence Zone (ITCZ) and its yearly oscillation that is responsible for the African monsoon. Two contrasted seasons characterize this site: (i) the dry season (mainly in winter, from December to March/April), with RH below 40%, when the ITCZ is the most distant from the site and (ii) the wet season (RH \approx 80%), mostly in summer (from June to September), while the ITCZ reaches latitudes close to those of Mbour.

The particles observed over the site can result from the combination of both local and transported aerosols depending on the movement of air masses induced by the meteorological conditions. In order to better understand the atmospheric context of the African site, we computed systematic back trajectories of air masses with the HYSPLIT model (Hybrid Single-Particle Lagrangian Integrated Trajectory). These back trajectories, ending at the observation site, reveal the history of air masses at three altitude levels (ground level, 3000 m, and 5000 m) along 72 h. Over the years 2006 to 2012, four computations have been processed per day (every 6 h). Similar patterns have been found between the different years. An example of the seasonally averaged results for 2006 is shown in Figure 1.

The distribution of the air masses features some privileged trajectories. The winter (dry season) can clearly be distinguished from the three others that present rather similar behavior. At this latitude, the global atmospheric circulation is governed by northeast dominating winds, namely, the Alizés, which behavior can be seen from the back trajectories in winter at the ground level; the Harmattan wind then transports Saharan air masses southwestward. Otherwise, from spring to autumn, the air masses at ground level are mostly originating from the northwest and more precisely from the west when focusing nearby the observation site. An illustration of the Ekman spiral can be observed for higher air masses as, mainly coming from the east, they are deviated from the ground direction.

On a finer time scale, one can note that the main changes in the wind orientation at the ground level occur in November and February. In-between of these months, lowest air masses come from the northeast and are under influence of the Saharan and Sahelian deserts. From March to October, a stronger oceanic influence is suggested by the back trajectories showing that the air masses have been transported along the coastline. During the same time period, the air masses at 3 km of altitude mainly come from the east and are, therefore, potentially loaded with dust particles. For the higher air masses (5 km of altitude), this eastern influence is shifted and shortened in time, from June to October. In January and February, the air masses at a range of 3 km are originating from the southeast regions, where active biomass burning fires occur in this period, due to the local agriculture [Pelon *et al.*, 2008].

Surface wind data, collected by the nearby-located weather station, reveal a good agreement with the trajectories study at ground level. Two main wind directions can be identified: one from the northeast for wintertime and another from the west for other seasons. Therefore, seasonal influences from oceanic and arid areas are also visible in the ground level meteorological observations.

Employment of Lidar and Sun photometer measurements for aerosol analysis requires cloudless observations. In order to ensure the representativeness of the remote sensing measurements for each season and, in particular, for the most cloudy summer, during the wet season, the cloud cover fraction has been investigated through the Lidar automatic cloud detection procedure developed during this work.

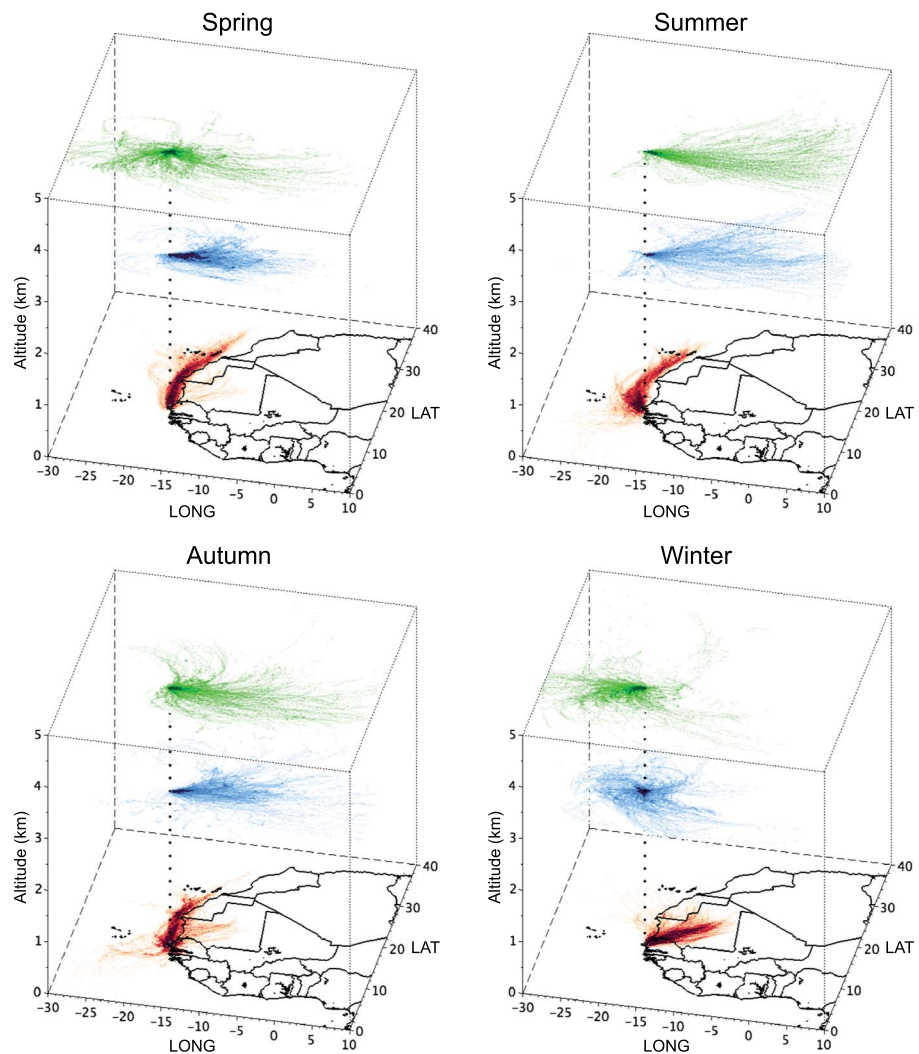


Figure 1. Seasonally averaged back trajectories processed over 72 h and finishing at Mbour at ground level (red), 3000 m (blue), and 5000 m (green) for 2006. The color intensity is proportional to the number of back trajectories contained by pixel. The black dotted line follows the vertical of the observation site.

Indeed, the instrument operates continuously regardless of weather conditions and therefore contains clouds measurements. The main seasonal results are reported in Table 1. The minimum and maximum clouds fraction occurs, respectively, during spring (17%) and summer (36%). In summer, 29% of the clouds are low-level clouds

Table 1. Clouds Cover Fraction Estimated With Lidar Automatic Detection for Each Season (%)^a

	Spring	Summer	Autumn	Winter
Clouds cover fraction	17.0	36.4	30.1	28.9
Daytime	38.7	43.8	48.0	45.3
Nighttime	61.3	56.2	52.0	54.7
Low altitude	12.2	29.2	15.7	9.7
Medium altitude	33.8	25.8	28.5	10.9
High altitude	54.0	45.0	55.8	79.4
Sunshine (h/d)	10.7	8.9	7.9	8.0

^aDistinctions regarding daytime and height-base clouds, according to the ISCCP (low, high, and medium altitudes stand, respectively, for clouds whose base is below 2 km, above 5 km, or in between), are also provided. The sunshine duration is calculated as the product between the clouds cover fraction and the length of the day.

according to the International Satellite Cloud Climatology Project (ISCCP) classification since their base is below 2 km of altitude. It is notable that this class of clouds is the less frequent in winter (10% of the total clouds), while most of the clouds are high-level clouds (79%). The sunshine duration has been calculated by multiplying the cloud cover fraction by the daylight duration. The obtained annual amount is reaching about 3200 h, which is in good agreement with the national weather measurements. The sunshine durations of 8.0, 10.7, 8.9,

and 7.9 h/d have been calculated for the different seasons from winter to autumn. Despite that the maximum of the cloud fraction is found during summer, this season is also characterized by the longest daylight duration. This compensation, therefore, enables a sufficient sunshine duration in the summer time. According to this interplay between daylight and cloud cover fraction, the autumn is the season that presents the shortest sunshine duration. Nevertheless, close to 8 h/d, this one is still sufficient to provide representative measurements of clear sky, as is also confirmed by the number of AOT measurements (20% of the total measurements). One could note that this number of AOT measurements is 35% higher during winter than during autumn, while the sunshine duration is rather similar for these two seasons. This difference can be explained by the fact that most of the clouds detected with the Lidar during the winter are high-level clouds, for which the detection from the Sun photometers is less sensitive [Chew *et al.*, 2010].

3.2. Column-Integrated Properties

In this part, we present a description of the different total column-integrated aerosol properties over different time scales.

3.2.1. Aerosol Optical Thickness

The seasonal contrast observed in the back trajectories is also present in the AOT observations, as indicates the AOT annual cycle (Figures 2a and 2b). For the sake of consistency with the Lidar wavelength, the AOT has been calculated at 532 nm using the wavelength dependence given by α .

An average (\pm standard deviation) of about 0.43 ± 0.29 has been calculated over the whole continuous observation period, from 2003 to 2014, considering more than 106,000 level 2.0 observations. In comparison, for Agoufou site (Tombouctou, Mali), which is located at the same latitude as Mbour, but distant from the coast by 2000 km, the respective average is about 0.52 ± 0.13 . These large average values and standard deviations indicate an important load of particles with a wide discrepancy. Most of the measurements (67% of daily averages) are between 0.1 and 0.5. A few clear days can be observed since 3% of the days are associated with a daily average lower than 0.1. At the opposite, 9% of the days are related to an AOT greater than 0.8. The yearly cycle reaches its maximum in summer and minimum in winter with respective averages of 0.57 ± 0.32 and 0.32 ± 0.21 (Table 2). Focusing on the monthly scale (Figure 2b), one can note that the maximum occurs in June with a median value around 0.57, following a local minimum in May (0.38 while the median is 0.41 in April). December appears as the clearest month of the year with a median of about 0.24. When one reduces the time scale study to the day basis (Figure 2c), a cycle can also be observed. From 09:00 to 17:00, the AOT is very stable since the medians are between 0.33 and 0.36. Nevertheless, higher values are measured in the beginning and the end of the day (0.41 at 08:00 and 0.50 at 19:00).

In order to investigate a potential of the long-term trends, we used the statistical Mann-Kendall seasonal test. With a significance of 95%, only a decrease of AOT has been found during autumn. The linear regression applied to the seasonal measurements provides a quantification of this decrease, which is about -29% between 2003 and 2014 ($-2.7\%/yr$).

3.2.2. Angstrom Exponent

Overall average of α as low as of 0.37 ± 0.25 indicates that the coarse mode is dominating. This is consistent with the influence by both dust and sea salt particles suggested by the air mass backward trajectories and by some in situ measurements [Deboudt *et al.*, 2010]. This average is nevertheless slightly greater than the one related to Agoufou site (0.30) that is closer to the dust emission sources and is probably less affected by deposition of the coarsest desert particles. An annual cycle, whose amplitude is about 60%, is observed in an opposite phase to the AOT cycle (Figures 3a and 3c). The minimum and maximum values measured during summer and winter are, respectively, 0.23 ± 0.20 and 0.48 ± 0.27 (see Table 2). In Figure 3c, the evolution of α at the daily scale again reveals an opposite cycle to the one observed for AOT. A weak variability is observed between 09:00 and 17:00 (medians spreading from 0.30 to 0.35), while lower values are observed at sunrise (0.25) and sunset (0.17). Unlike for the AOT, no trends can be highlighted for any season with the seasonal Mann-Kendall test with a significance of 95%.

3.2.3. Volume Size Distribution

In this part we study the time variability of the VSD through the three following parameters: the effective radius of the fine (r_{fine}) and the coarse (r_{coarse}) mode of a bimodal size distribution, and the ratio of the amplitude of these two modes $n_{0,c}/n_{0,f}$, where $n_{0,c}$ and $n_{0,f}$ stands, respectively, for the maximum of the coarse

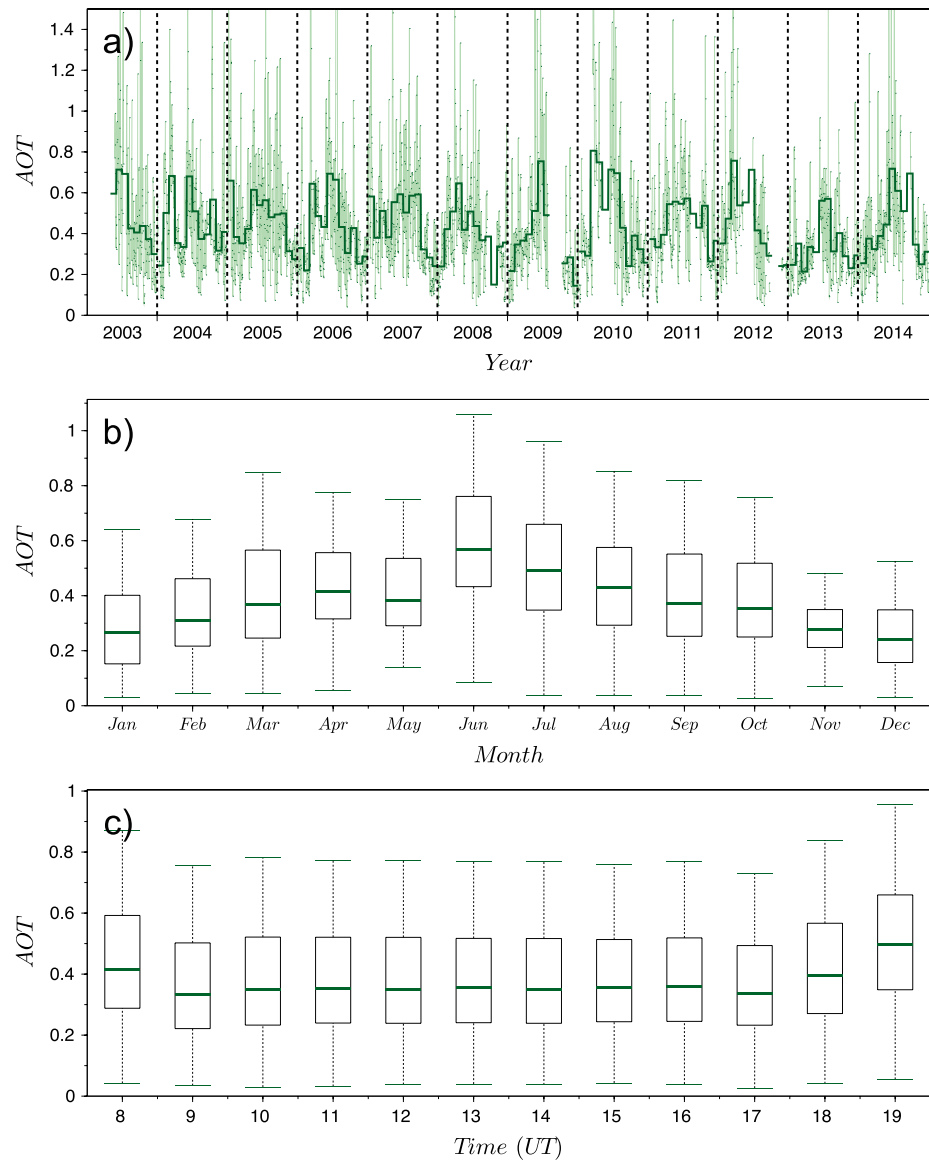


Figure 2. Aerosol optical thickness measured at Mbour and interpolated at 532 nm. (a) The time series shows daily averages (light green) and monthly averages (dark green) of the parameter. (b and c) Boxplots for different time scales. The boxes extend from the first to the third quartile (IQR). The colored line is the median. Whiskers, highlighting variability, extend from minimal and maximal values include in (median-1.5 IQR; median + 1.5 IQR).

mode and the fine mode. Unlike AOT and α that are derived from direct Sun measurements, retrieval of the VSD is normally conditioned by observations of sky radiances and requires large solar zenith angles and measurements at several scattering angles. This is why the inversion results cannot be provided at the latitude of this site between about 12:00 and 15:00 UTC.

3.2.3.1. Effective Radii

The effective radii of the fine and the coarse modes [Schuster *et al.*, 2006] present seasonal cycles with a similar amplitude (about 10%) but with opposite phases. Thus, the maximum of r_{coarse} occurs simultaneously with the minimum of r_{fine} in December–January ($r_{\text{coarse}} = 1.85 \mu\text{m}$ and $r_{\text{fine}} = 0.12 \mu\text{m}$). An inverse pattern is observed in August–September ($r_{\text{coarse}} = 1.65 \mu\text{m}$ and $r_{\text{fine}} = 0.14 \mu\text{m}$). In contrast with the previously described parameters, there is no evident daily cycle for any mode of the VSD. On the other hand, the application of the seasonal Mann-Kendall test highlights opposite trends for the two radii. A decrease in r_{fine} of about 1.7%/yr (from $0.16 \mu\text{m}$ to $0.13 \mu\text{m}$) can be noted in spring, while r_{coarse} increases by about 0.8%/yr

Table 2. Main Vertical-Integrated Aerosol Properties for Different Seasons, Mass Concentration Measured at Ground Level by a TEOM, and Vertical Distribution Parameters Retrieved From Lidar Measurements (Average \pm Standard Deviation) Over the Period 2006–2014

	Spring	Summer	Autumn	Winter
AOT	0.48 \pm 0.30	0.57 \pm 0.32	0.37 \pm 0.23	0.32 \pm 0.21
α	0.31 \pm 0.18	0.23 \pm 0.20	0.46 \pm 0.25	0.48 \pm 0.27
r_{fine} (μm)	0.14 \pm 0.03	0.14 \pm 0.03	0.13 \pm 0.02	0.13 \pm 0.02
r_{coarse} (μm)	1.72 \pm 0.17	1.69 \pm 0.14	1.75 \pm 0.20	1.82 \pm 0.24
$n_{0,c}/n_{0,f}$	10.22 \pm 6.19	13.00 \pm 6.06	7.06 \pm 5.72	6.24 \pm 5.57
ϖ_0	0.92 \pm 0.02	0.94 \pm 0.02	0.92 \pm 0.04	0.87 \pm 0.05
m_r	1.46 \pm 0.04	1.47 \pm 0.04	1.45 \pm 0.05	1.43 \pm 0.05
m_i	0.004 \pm 0.002	0.003 \pm 0.001	0.005 \pm 0.004	0.010 \pm 0.007
S_a (sr)	27 \pm 13	37 \pm 21	37 \pm 18	30 \pm 15
PM_{10} ($\mu\text{g m}^{-3}$)	145 \pm 153	56 \pm 29	75 \pm 57	149 \pm 107
$\sigma_{\text{ext}}(z_0)$ (km^{-1})	0.21 \pm 0.13	0.21 \pm 0.14	0.13 \pm 0.09	0.15 \pm 0.12
$\sigma_{\text{ext}}(3 \text{ km})$ (km^{-1})	0.08 \pm 0.06	0.09 \pm 0.06	0.07 \pm 0.05	0.04 \pm 0.04
PBL (m)	730 \pm 540	790 \pm 550	880 \pm 670	960 \pm 640
TL (m)	3790 \pm 1380	3320 \pm 1710	3040 \pm 1400	2690 \pm 1430

(from 1.64 μm to 1.90 μm). An increase in r_{coarse} is also found during winter (1.3%/yr, from 1.67 μm to 1.90 μm). The observed trends can be however quite unstable keeping in mind that an accuracy of about 35% can be expected for these retrievals parameters under the dust condition [Dubovik *et al.*, 2000].

3.2.3.2. Modes Proportion

The monthly averaged amplitude of the coarse mode is at least twice greater than the one of the fine mode. The overall average of the ratio $n_{0,c}/n_{0,f}$, which is plotted for different time scales in Figure 4, is about 9.7 ± 6.1 . The parameter has a strong seasonal cycle. It reaches its maximum in summer ($n_{0,c}/n_{0,f} > 13$) and its minimum in winter (≈ 6 , cf. Table 2). Namely, the minimum of the ratio occurs in November and December with median values below 3. Despite only a part of the daily cycle can be observed due to the retrievals limitation to the large Sun angles, the data suggest a reduction of about 18% at midday. That is, at 08:00 and 19:00, $n_{0,c}/n_{0,f}$ is above 10, while it is below 7 at 10:00 and 16:00. No long-term trend has been found over the whole time series.

For the sky measurements corresponding to $\text{AOT} \geq 0.4$ at 440 nm, which are common to this highly loaded site, the Sun photometer inversions provide aerosol optical properties such as the refractive index RI and the single-scattering albedo ϖ_0 .

3.2.4. Single-Scattering Albedo and Refractive Index

3.2.4.1. Single-Scattering Albedo

Figure 5 shows the ϖ_0 on different time scales. The value is presented at the Lidar's wavelength (532 nm) and is a result of interpolation between 440 nm and 670 nm that are available as part of the AERONET inversion products. The overall average is about 0.92 ± 0.04 . It shows a pronounced seasonal cycle, with maximum and minimum, respectively, in summer and winter. This cycle, which was already noted in Léon *et al.* [2009] for the period of 2006–2008, is visible for every single year of the period of 2003–2014 analyzed here. The maximum reaches 0.94 (± 0.02) in summer and the minimum, associated to stronger absorption, is about 0.87 (± 0.05) in winter, namely, a relative variation of about 4%. This pattern is consistent with measurements performed during some field campaigns [Osborne *et al.*, 2008] that indicate a mixture of dust and biomass burning particles in winter [Pelon *et al.*, 2008]. The daily scale reveals a cycle similar to the one of the ratio $n_{0,c}/n_{0,f}$ which seems to reach its lowest value at midday, while the variability becomes more important (see Figure 5c). No long-term trend could have been noted for any season.

3.2.4.2. Refractive Index

The real and the imaginary parts of the refractive index, calculated at 532 nm, present inverse seasonal cycles. As expected, m_i is in opposite phase with ϖ_0 . The extreme values are observed during winter (0.010) and summer (0.003). Reciprocally, m_r seasonal averages are around 1.43 in winter and 1.47 in summer. The seasonal averages and standard deviations are reported in Table 2. A daily trend has been found mainly for m_i . This parameter increases from 08:00 to 10:00 UTC (from 0.003 to 0.005) and decreases from 16:00 to 18:00 (from 0.007 to 0.002). This constitutes a portion of cycle that is significant since its peak-to-valley value,

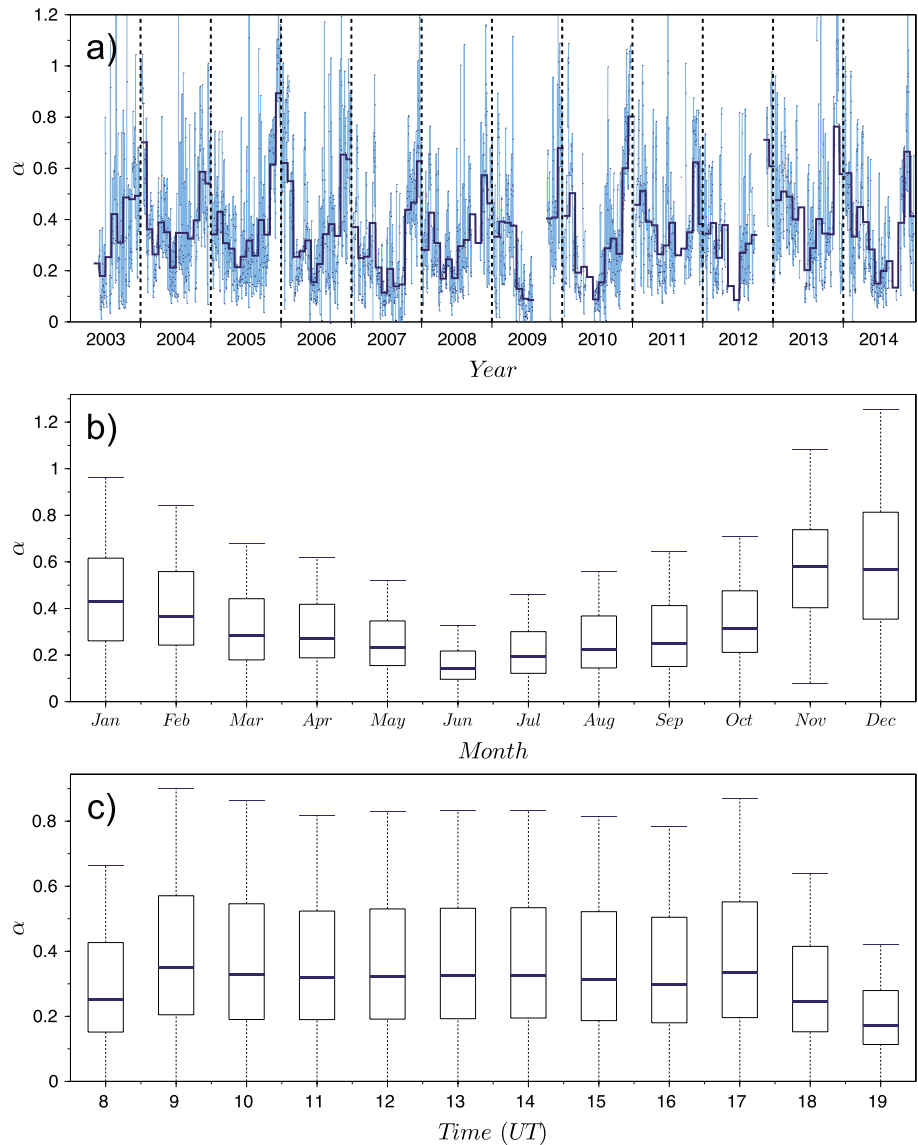


Figure 3. Same as Figure 2 but for Angstrom exponent.

of about 120%, is greater than the expected accuracy (50%) [Dubovik et al., 2000]. Application of the seasonal Mann-Kendall reveals no trend for m_i , neither for m_r , which is in line with the results for τ_{0} .

The last column-integrated parameter presented in this part is the Lidar Ratio and is derived from the conjoint inversion of Sun photometer and Lidar measurements.

3.2.5. Lidar Ratio

Between 2006 and 2014, more than 39,000 inversions distributed over 1564 days have successfully passed the quality control tests discussed in section 2.2. Number of Lidar ratio values related to dust particles can be found in the literature. Most of them are nevertheless based on time-limited field campaigns. Thus, as a nonexhaustive list, one can cite works of Esselborn et al. [2009], Powell et al. [2000], Voss et al. [2001], and Welton et al. [2000] with respective averaged values of 44 ± 6 sr, 35 ± 5 sr, 41 ± 8 sr, and 37 ± 9 sr at 532 nm. Papayannis et al. [2008] present a climatology of transported dust S_a retrievals over several years with Lidars integrated into the European Aerosol Research Lidar Network. A high variability is found (20–100 sr), which can be partially explained by the variable distance of the observation sites from the sources. Indeed, the particles properties are affected by their transport through different processes such as the humidification or the deposition of the coarsest particles. In our study, an average of $S_a = 32 \pm 16$ sr is found. This result is

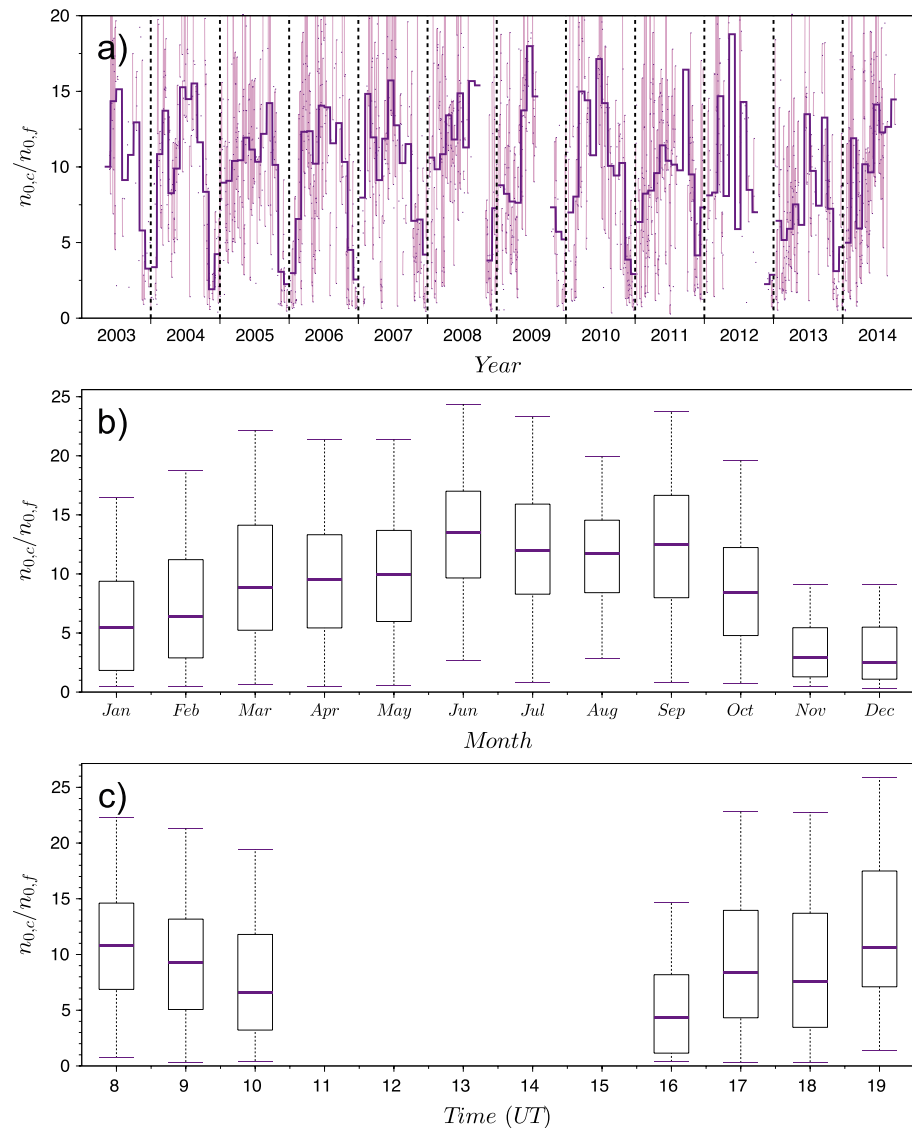


Figure 4. Same as Figure 2 but for the ratio of coarse and fine modes amplitude.

therefore consistent with published values. However, one can notice that in spite of the attention dedicated to the Lidar calibration, higher values are observed after 2011, when the calibration is more trustable according to the authors. Starting from this time, an averaged value of $S_a = 40 \pm 15$ sr has been found.

Unlike most of the previously described parameters, no clear seasonal cycle is found in the Lidar ratio. Thus, the intrusion of biomass burning particles during winter does not seem to affect consequently the column S_a . However, by filtering cases according to the Angstrom exponent in order to favor fine particles, an increase of S_a with α can be observed. After 2011, we thereby have $S_a(\alpha > 1.0) = 46 \pm 19$ sr and $S_a(\alpha < 0.5) = 39 \pm 15$. The presence of sea salts, suggested at ground level by the back trajectories from spring to autumn, would tend to decrease the Lidar ratio (compared to pure dust cases) since the low values of S_a (≈ 25 sr) are attributed to the marine particles [Müller et al., 2007].

In the 3 years study presented by Léon et al. [2009], the discussed Lidar ratio is calculated from the Sun photometer retrievals. Indeed, $S_{a,Sun}$ is defined as follows:

$$S_{a,Sun} = \frac{1}{\varpi_0} \frac{4\pi}{\rho(180)}, \tag{1}$$

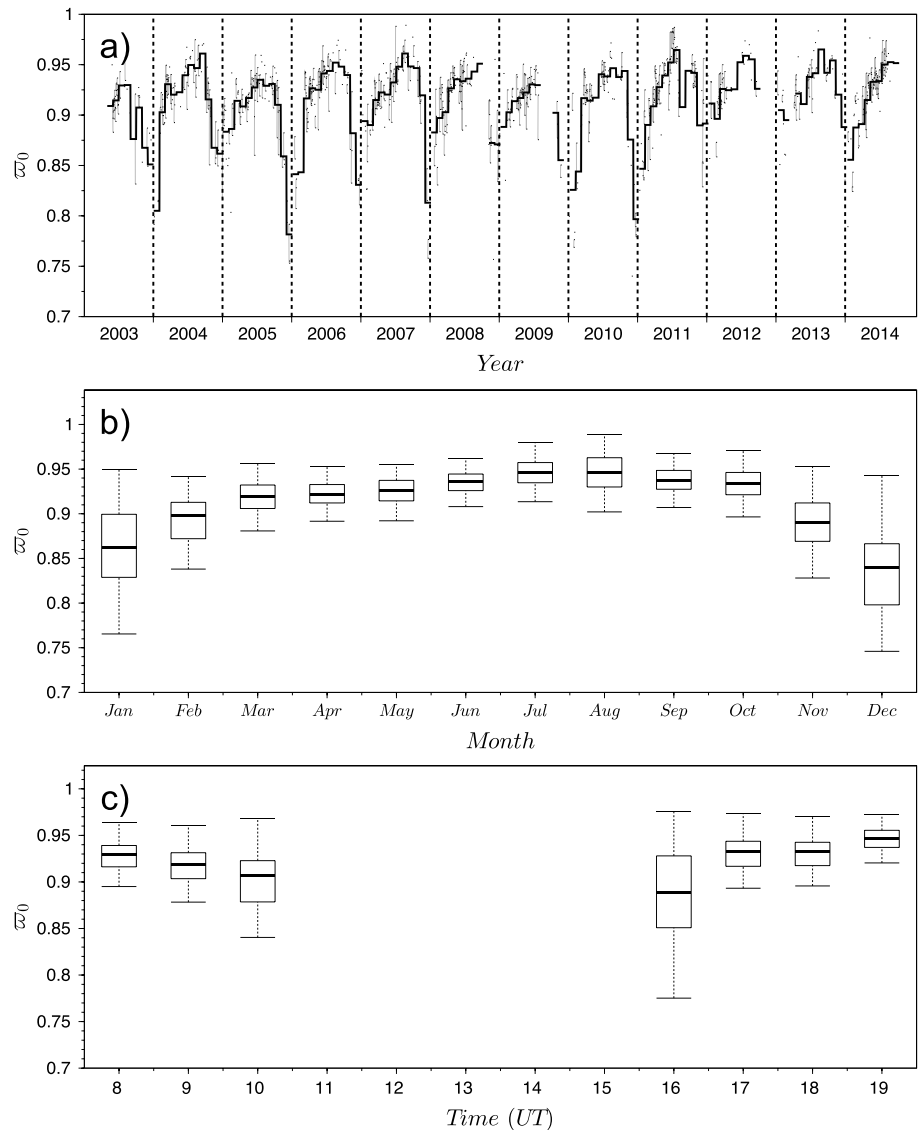


Figure 5. Same as Figure 2 but for the single-scattering albedo ω_0 .

where $p(180)$ is the phase function at 180° . The calculation of $S_{a,Sun}$ over the whole data set gives an average value of about 63 ± 11 sr. In this case, a seasonal cycle is clearly visible with the winter values (≈ 75 sr) higher than the summer ones (≈ 50 sr). With respect to the Lidar ratio climatology as calculated from Sun photometers retrievals [Catrall *et al.*, 2005], the high winter values could be attributed to urban/biomass burning particles, while the low summer average is mainly consistent with dust/sea salts.

Because ω_0 is required in $S_{a,Sun}$ calculation, the reported averaged values are relevant for AOT > 0.4 at 440 nm. In the same conditions, the averaged S_a increases from 40 ± 15 to 44 ± 11 sr. This value is still lower than the global $S_{a,Sun}$. Such differences between Lidar and photometric Lidar ratios have been found by Müller *et al.* [2007] who highlight that due to geometric configuration, the phase function is not directly measured by the Sun photometer at 180° but is computed. On the other hand, the Lidars are less sensitive to the lowest particles (overlap function, extrapolation for the first meters) and could be less affected by the freshly emitted aerosols. On the daily scale, we observe higher values of S_a at 10:00 and 16:00 (30 sr and 29 sr) comparing to the beginning, the middle, and the end of the day (27 sr at 08:00 and 18:00 and 26 sr at 14:00). The amplitude of this trend is nevertheless quite low regarding the variability of this parameter.

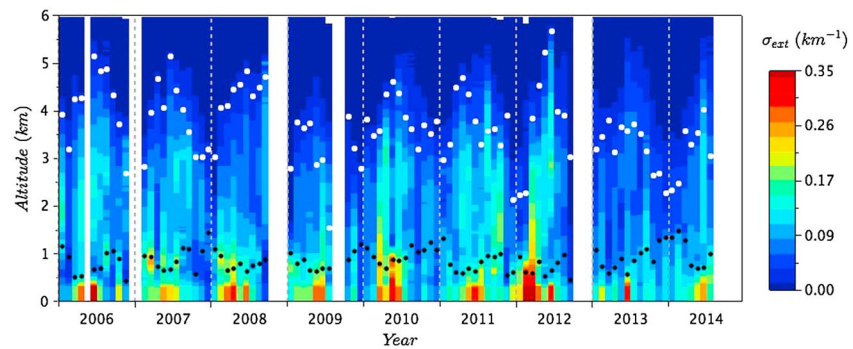


Figure 6. Time series of monthly averaged extinction profiles. The white and black dots refer, respectively, to the heights of the planetary boundary layer and the top layer.

3.3. Vertical Distribution

A time series of the monthly averaged vertical extinction profiles, PBL, and TL heights is shown in Figure 6. The maximum values are observed at ground level, usually in the midyear (summer), reaching 0.35 km^{-1} at 532 nm. Significant extinction values ($\sigma_{\text{ext}} > 0.1 \text{ km}^{-1}$) are observed under the TL ranging from 2.5 km in winter to 5 km in summer. The PBL variation is weaker and does not exceed 500 m. It is not correlated with the seasonal temperature, as it can be observed in some midlatitudes areas [Seidel *et al.*, 2010]. Lower values are even observed in spring and summer (730 m and 790 m), while the PBL is the most extended in winter (960 m).

Despite the interannual variability, some trends can be featured regarding the vertical distribution of the aerosols. The seasonal averages are presented in Figure 7, and the averages of some key parameters are reported in Table 2.

The winter is characterized by a relatively monotone decrease of the extinction with the altitude. The seasonal average is about $\sigma_{\text{ext}}(z_0) = 0.15 \text{ km}^{-1}$ at ground level, while it is about 0.04 km^{-1} at 3 km. The relative decrease, therefore above 70%, illustrates the transport of the dust from the desert sources at ground level as suggested by the back trajectories. The absence of separate elevated layers does not permit to highlight sporadic biomass burning particles events from the seasonally average profiles.

During springtime an increase of extinction values at ground level is observed (+50%). The increase reaches more than 125% at an altitude of 3 km. These growths are coincident with the transport of marine particles at the ground level and of dust in altitude (Figure 1).

Similar extinction values are observed in summertime at ground level and slightly higher values at a height of 3 km. An uplifted layer (Saharan Air Layer) is clearly visible as transported above the PBL. At a height of 5 km, the extinction grows from 0.01 km^{-1} in spring to 0.03 km^{-1} in summer. Finally, it is noticeable that the interannual variability is quite low for this season compared to spring or autumn. The westward transport of this elevated layer is regularly observed in Capo Verde [Chiapello *et al.*, 1997] and over Canary Islands [Kandler *et al.*, 2007; Viana *et al.*, 2002].

The lowest extinction values at ground level are found in autumn (0.13 km^{-1}). The decrease is also important at altitude of 5 km where σ_{ext} does not exceed 0.02 km^{-1} , excluding the year 2008, which average relies on measurements spread over four different days only. Important extinctions are however still observed at 3 km. The associated back trajectories consistently reveal a residual contribution from the source regions at this altitude.

The annual cycle of TL, whose amplitude is beyond 1000 m, tracks the top of the Saharan Air Layer during summer and is a signature of the desert particles transport on altitude [Léon *et al.*, 2009].

3.4. Interpretation

This section presents interpretation of the aerosol properties variability on the different time scales as measured by the Sun photometer (integrated parameters), the TEOM (PM_{10}), and the Lidar (vertical distribution) collocated on the observation site. The meteorological parameters, as temperature, pressure, wind, and precipitations, are also considered in the interpretation of the different features previously described.

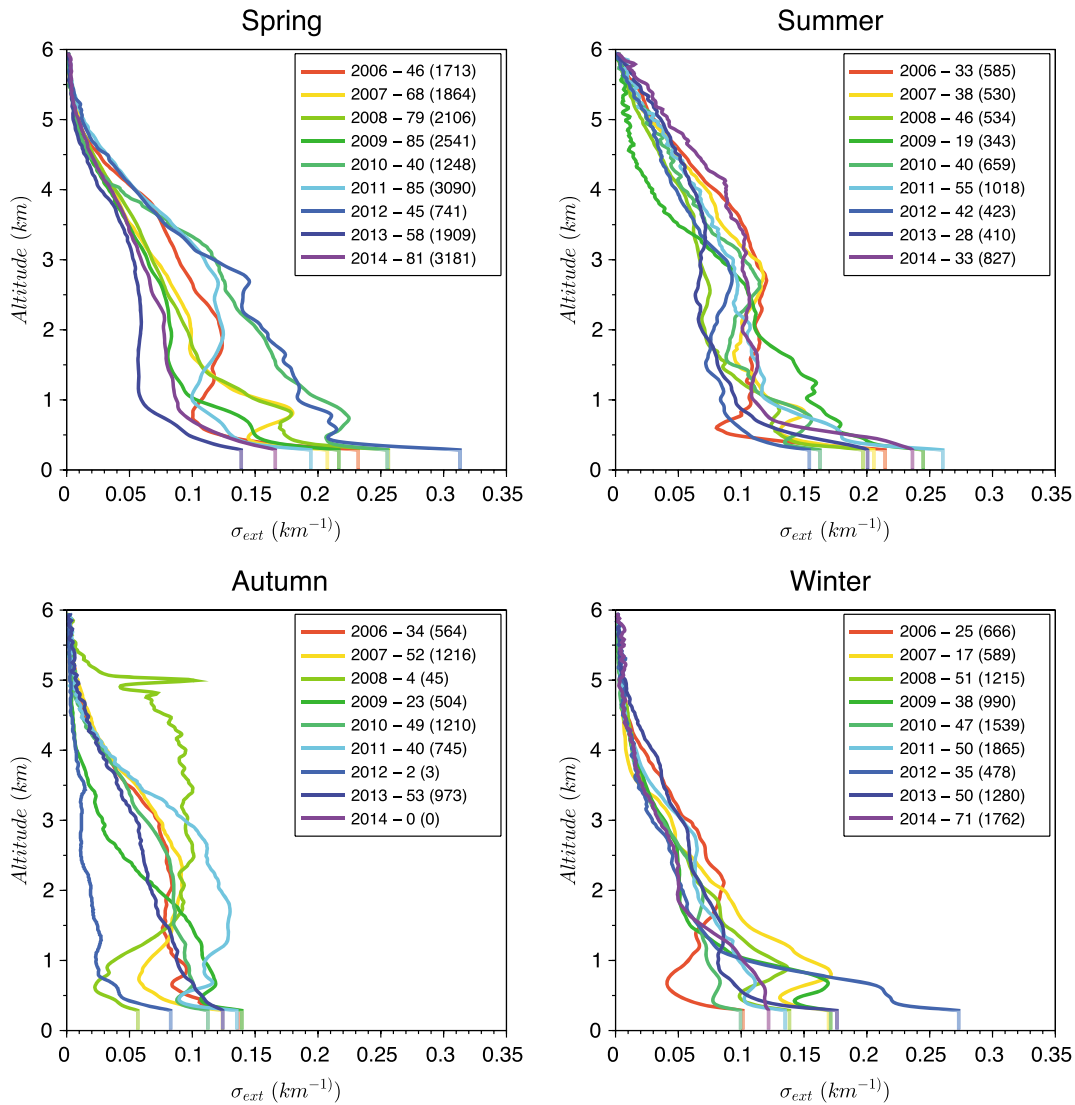


Figure 7. Seasonally averaged extinction profiles for different years. Beside each year, the numbers of different days available and, in parentheses, the total number of inversions for this period.

3.4.1. Seasonal Trends

The study of the integrated aerosol properties on the seasonal scale reveals mainly two contrasted seasons: the summer (wet season) and the winter (dry season) spaced out by the intermediate spring and autumn. The annual cycles observed for most of the parameters, with different relative amplitudes, are either in phase or in opposition of phase. The profiles describing the vertical distribution of the aerosols present also different seasonal features.

The summer is characterized by a large bulk of aerosols (maximum of AOT) of coarse size as indicated by the low α and the maximum of the ratio $n_{0,c}/n_{0,f}$ and moderate absorption ($\tau_{0,0.94}$) that corresponds to the low imaginary part of the refractive index, m_i (0.003). These values are consistent with desert-dust particles. The presence of sea salts, suggested by the back trajectories at ground level is nevertheless not discordant with the seasonal averages. Indeed, the climatology value reported by *Dubovik et al.* [2000] for desert dust and oceanic particles (in Capo Verde) is about $\tau_{0,0.94} = 0.95$ at 532 nm. The complex refractive index of about $m = 1.47 - 0.003i$ is still consistent with a mixture of dust and sea salts in Mbour during summer. Logically, summer is associated with the highest relative humidity ($\approx 75\%$), which however should not affect significantly the optical properties of the dominant dust [*Gassó et al.*, 2003], including the extinction, and cannot explain the

highest seasonal AOT. This large AOT is induced by the large σ_{ext} retrieved above the PBL, which shows the transport of dust in elevated layers that was suggested by the back trajectories [Chiapello *et al.*, 1995]. This transport in altitude is also responsible for the lowest mass concentration measured during this season (Table 2).

The winter is associated with a much lower aerosol loading. The maximum seasonal value of α (and the minimum $n_{0,c}/n_{0,f}$) implies a stronger contribution of the fine particles. However, the VSD remains dominated by the coarse mode. These particles are absorbing, as indicated by the minimum κ_0 (0.87) linked with the high values of the imaginary part of the refractive index, m_i (0.010). The values are consistent with a mix of both desert dust and biomass burning aerosols [Derimian *et al.*, 2008a, 2008b]. Indeed, the κ_0 found is in close agreement with the climatology value for biomass burning particles from the African savanna [Dubovik *et al.*, 2000] which is about $\kappa_0 = 0.87$. This confirms the origin of the absorbing particles observed over Mbour. The averaged α , although maximum during this season (0.48), is however much lower than the one associated with African savanna biomass burning particles ($1.4 < \alpha < 2.2$) and reveals the presence of coarse particles. As mentioned previously, this season coincides with vegetation fires initiated for agriculture purposes [Liousse *et al.*, 2010]. Some biomass burning events have been studied in this area at this period: Pelon *et al.* [2008] at Djougou (Bénin) or Cavalieri *et al.* [2010] at Banizoumbou (Niger), Cinzana (Mali), and even at Mbour, for the three first years of observation. Nevertheless, a recent study based on in situ measurements (aromatic composition) performed during the dry season in Mbour shows that the organic particles come mainly from local sources (wood-fired oven, burning of grass/dry leaves), rather than the transport of biomass burning particles coming from Sahelian area [Flament *et al.*, 2011]. The local emission of these particles in the lowest layers could explain why no separate elevated layer, which would represent the biomass burning particles transport, is found in the seasonal averaged extinction profiles.

In Mbour, the temperature difference is weak between winter (26°C) and summer (29°C). The minimum of PBL height observed during summer could be explained by the more important scavenging due to higher precipitations, leading to a more efficient cleaning of the lowest layers.

In the summertime, the mass-to-extinction ratio of the particles measured at low level is 4 times weaker than the one corresponding to winter, when the aerosols transported at this level mainly come from the desert sources. This difference may partially be attributed to a lower density for the summer aerosols, which is consistent with sea salts particles (comparing to dust, whose density is about 2.6 g cm^{-3}).

3.4.2. Daily Trends

All of the daily cycles previously described have been observed for each of the seasons, although with different magnitude. This indicates a steady and probably local phenomenon and not an artifact possibly produced by the number of measurements involved (e.g., more measurements early in the morning (~08:00) and later in the evening (~18:00) during the summertime).

The Angstrom exponent, α , presents lower values at the beginning and the end of the day occurring simultaneously with a higher $n_{0,c}/n_{0,f}$ ratio (compared to midday). This behavior is even more contrasted in autumn and winter (α cycles with amplitudes about 66% and 78%) comparing to spring and summer (30% and 13%). The variation of both α and $n_{0,c}/n_{0,f}$ is consistent and indicates finer particles at midday. This observation could result partially from an effect of aerosol hygroscopic growth since the RH is minimum at around 12:00 (~60%) and is maximal (~80%) at 06:00. In spring and summer, the higher proportion of mineral dust, less affected by the RH, would then explain the weaker observed cycles. This size cycle might be also explained by the previously mentioned local emission of carbonate aerosols during the day, most likely composed of fine particles. This latter hypothesis is reinforced by the two opposite cycles observed for κ_0 and m_i . Respective lower and higher values of κ_0 and m_i are found at sunrise and sunset. These features imply more absorbing particles at midday, which is consistent with the emission of carbonate (absorbing) aerosols.

The daily scale study also highlights a cycle of the AOT, which minimum is usually reached between 12:00 and 14:00. This trend has already been found in other sites (e.g., Nigeria), but the reasons are not always clear [Smirnov *et al.*, 2002]. In our case, for instance, the daily variability in AOT appears as correlated with one of wind speed. Wind speed values (downscaled to four averaged values per day) demonstrate that the wind is twice faster at 12:00 ($\sim 3 \text{ m s}^{-1}$) than at 18:00 or 06:00 ($\sim 1.5 \text{ m s}^{-1}$). This variation may imply an enhanced dispersion of the particles at midday, which could therefore induce a decrease of the aerosol concentration and a lower AOT.

It is noteworthy to mention that the site is affected by regular arrivals of the sea breeze, which are characterized by sudden changes of the wind direction, temperature that drops up to 10° within few minutes, and relative humidity. Therefore, although averaged meteorological parameters do not allow direct consideration of changes due to the sea breeze arrival, it may indeed affect the aerosol concentration and properties during the noontime.

The daily study of the vertical profiles has shown weak variation. Similarly to the seasonal scale, the differences of temperature during a day are generally low, since the maximum is observed between daytime and nighttime during the spring and is about 4°C on average. This relative thermal stability does not strongly stimulate the convection phenomena that, therefore, do not seem to rule the vertical distribution of aerosols in this site.

3.4.3. Weekly Trends

The weekly scale studies can be used, especially for urban sites, in order to demonstrate the anthropogenic impact when a correlation is found with the human activities rhythm—the “weekend effect” [Bäumer *et al.*, 2008; Jin *et al.*, 2005; Marr and Harley, 2002].

We focus on analysis of weekly variations of AOT, α , and PM_{10} . If no significant trend has been highlighted for α , a cycle has been found for AOT (about 7%) with minimums at the beginning and the end of the week, between which PM_{10} increases by about 10% (see supporting information). An anthropic effect seems to occur at this site, even though its atmospheric conditions are mainly driven by natural particles. Although Mbour cannot be considered as an active industrial city, some part of its 200,000 inhabitants use vehicles that are often decrepit. “If the government applied international standards, more than 90% of the vehicle fleet would be impounded,” declared the transport and infrastructure minister, Thierno Alassane Sall, in July 2013. In addition, an important north to south transportation axis passes through Mbour. The use of these high-emitting vehicles could explain the AOT observed cycle, as the transport is likely to be less important during the weekend. With low-averaged wind speed measured at ground level, the accumulation of the emitted particles from the transport is thereby strengthened, leading to an increase of PM_{10} during the week from Monday to Saturday.

3.4.4. Long-Term Trends

The application of the seasonal Mann-Kendall test revealed an important decrease of AOT during autumn since it reaches almost 30%. Not any simultaneous trend has been found for this season considering the other parameters and measurements. This decrease is therefore driven by an extensive parameter. We do not have an explanation for this behavior yet, which might be explored by further investigating the meteorological conditions in the source regions. A simultaneous decrease of r_{fine} has been found during spring with an increase of r_{coarse} that extends until winter. However, these trends remain weak as regards the expected accuracy on these parameters. The study of other parameters, as well as the back trajectories, could not provide an explanation for these behaviors.

4. SW Direct Radiative Effect and Heating Rates Calculated Using Lidar Profiles

The Mbour site is mainly influenced by mineral dust particles in summer and is sporadically subject to the transport of biomass burning particles during the wintertime. The aerosol radiative effect therefore involves particles of different type [Derimian *et al.*, 2008a, 2008b]. In contrast to previous studies, the aerosol radiative effect calculations in this work involve the aerosol vertical profiles derived from the Lidar observations. The vertical aerosol distribution may influence the calculated aerosol radiative effect, particularly in specific combination with surface reflectance, aerosol loading, and absorption properties, [e.g., Guan *et al.*, 2010]. Disposing of long time series of extinction profiles, we present the results of the shortwave (0.2 to 4 μm) direct radiative effect calculated for the whole observation period employing both Lidar and Sun photometer observations.

4.1. Definitions

The direct net radiative effect (ΔF_{net} , denoted ΔF hereafter) is defined as the difference between the net fluxes (difference between downward and upward fluxes) for an atmosphere containing aerosols, F^A , and aerosol free atmosphere, F^C , e.g., [García *et al.*, 2012; Roger *et al.*, 2006]:

$$\Delta F = (F^{\downarrow A} - F^{\uparrow A}) - (F^{\downarrow C} - F^{\uparrow C}) \quad (2)$$

where the arrows \uparrow et \downarrow indicate, respectively, upward and downward fluxes.

At the bottom/top of atmosphere (BOA/TOA), the respective radiative effects, ΔF_{BOA} and ΔF_{TOA} , are defined as follows:

$$\Delta F_{\text{BOA}} = \left(F_{\text{BOA}}^{\downarrow A} - F_{\text{BOA}}^{\downarrow C} \right) (1 - SA), \quad (3)$$

where SA is the surface albedo, and

$$\Delta F_{\text{TOA}} = \left(F_{\text{TOA}}^{\uparrow C} - F_{\text{TOA}}^{\uparrow A} \right). \quad (4)$$

The difference between the radiative effects at TOA and BOA gives the atmospheric radiative effect, ΔF_{atm} , which corresponds to the residual radiative fraction into the atmosphere:

$$\Delta F_{\text{atm}} = (\Delta F_{\text{TOA}} - \Delta F_{\text{BOA}}) \quad (5)$$

A positive radiative effect therefore indicates a heating of the surface-atmosphere system, while a negative value implies a cooling.

In order to study how efficient are the aerosols regarding the radiative effect, the radiative efficiency is introduced, ΔF^{eff} , which allows to get rid of the variable quantity of particle. It is therefore defined as the net radiative effect per unit of AOT, e.g., at 550 nm:

$$\Delta F^{\text{eff}} = \frac{\Delta F}{\text{AOT}_{550}}. \quad (6)$$

Finally, the radiative effect can be used for calculating the heating rate, $\frac{dT}{dz}$ (K d^{-1}), which is proportional to its vertical derivative and is defined as follows:

$$\frac{dT}{dt} = -\frac{1}{c_p \rho} \frac{dF}{dz}, \quad (7)$$

where c_p is the mass thermic capacity ($\text{J} \cdot \text{kg}^{-1} \cdot \text{K}^{-1}$) and ρ the air density (1293 kg m^{-3}).

4.2. Methodology

The radiative effect calculation is performed over the whole database, whenever both Sun photometer and Lidar inversions are available. Thus, we dispose of an accurate aerosol model (spectral refractive index, VSD, and nonsphericity fraction) and a measured profile of extinction. A computational tool that is implemented in the AERONET operational code for calculations of broadband solar flux and aerosol radiative effect [García *et al.*, 2008] is then applied for results of the combined Sun photometer and Lidar measurements. A real extinction profile is therefore attributed to every AERONET retrieval and is taken into account in the aerosol radiative effect calculation. As have been described in Derimian *et al.* [2008a, 2008b, 2012] and García *et al.* [2008, 2012], the radiative effect computational tool employs the GAME radiative transfer model (Global Atmospheric Model) [Dubuisson *et al.*, 1996, 2006]; Roger *et al.*, 2006] that enables to accurately account for the molecular scattering and the gaseous absorption. The water vapor amount is estimated thanks to the differential absorption measured at $0.94 \mu\text{m}$ with the Sun photometers (AERONET inversion). Standard profiles are used in order to describe the CO_2 . Monthly climatology values of the total ozone content obtained from NASA Total Ozone Mapping Spectrometer are used for the ozone vertical profiles. The radiative code also takes into account variability in the surface reflectance and its directionality. To that end, the surface reflectance is approximate by using a bidirectionnal reflectance distribution function as characterized by the albedo surface modeled from MODIS climatology.

The radiative effect calculation is performed at several zenithal angles. The following interpolation then permits assessment of the daily radiative effect, which is the object of this study. The logistics of the calculation process is summarized in Figure 8.

4.3. Radiative Effect

4.3.1. Results

The monthly averaged profiles of the aerosol net radiative effect are shown in Figure 9. Seasonal averages are also reported in Table 3 for key parameters. The results reveal a clear seasonal cycle. Focusing at low altitudes, we observe the highest absolute values during the spring ($\Delta F_{\text{BOA}} = -24.47 \text{ W m}^{-2}$) and the lowest during the winter ($\Delta F_{\text{BOA}} = -17.19 \text{ W m}^{-2}$), which to say a relative difference of about 30%. At TOA, the minimum is observed in winter ($\Delta F_{\text{TOA}} = -5.13 \text{ W m}^{-2}$), and the maximum is related to summer ($\Delta F_{\text{TOA}} = -11.58 \text{ W m}^{-2}$).

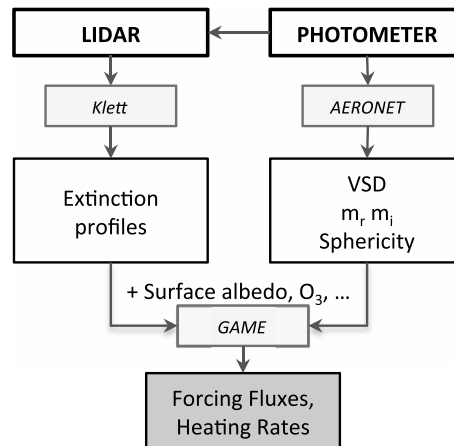


Figure 8. Aerosol radiative effect calculation logistics.

The absolute difference of about 6.5 W m^{-2} is, at this altitude, greater than the one observed at ground level (5.5 W m^{-2}). The resulting atmospheric effect is maximum during spring and minimum during autumn.

These results are modulated by the amount of particles, which vary widely as shown by the seasonal AOT cycle. The efficiency, ΔF^{eff} , permits to get rid of this effect. Figure 10 presents the values at TOA and BOA, as well as the surface albedo used for the calculation.

The annual variation of the surface albedo in this site is not strong but

still visible (between 0.15 and 0.21) and can explain a part of the TOA aerosol radiative effect variability. In contrast to ΔF , a maximum of ΔF^{eff} at ground level is found during winter (a mean value of -65.23 W m^{-2}). The minimum of ΔF^{eff} of about -45.19 W m^{-2} is reached in summer. This value is consistent with the work of Garcia et al. [2012] that is associated with the dust particles. The annual cycle at TOA is out of phase with the one at BOA. The maximum and minimum are thus observed, respectively, in autumn and spring for a relative difference of about 40%.

The maximum of radiative effect, observed during spring to summer at BOA, is therefore due to the highest concentration in particles. Associated with a low absorption, the desert dust that dominates during these seasons is indeed less efficient than the strongly absorbing particles observed during winter, known as influenced by the biomass burning aerosols [Haywood et al., 2008].

Because desert dust is large enough to interact with the terrestrial radiation and has a positive effect globally, it is balancing the shortwave negative forcing [Haywood and Boucher, 2000]. The longwave aerosol radiative effect, however, is not in the scope of the current study.

4.3.2. Influence of the Aerosols Vertical Distribution

Whenever the vertical distribution of the aerosols is unknown, simple models can be used (exponential, Gaussian, etc.). In order to estimate an uncertainty committed by using such simplifications, the broadband radiative fluxes have been calculated using vertical profiles retrieved by the Lidar and profiles approximated by a Gaussian distribution centered at a height of 2 km and with a standard deviation of 500 m; the rest of the aerosol characteristics are evidently the same in the both scenarios. The obtained differences are reported in Table 3.

For any season, the uncertainties obtained for the radiative effect at BOA are negligible ($<0.5\%$). It is however somewhat larger for the case at TOA, where a seasonal variability is also observed. The minimum differences occurred in summer (2%) and the maximum in winter (5%). The reason for this seasonal variability is that an

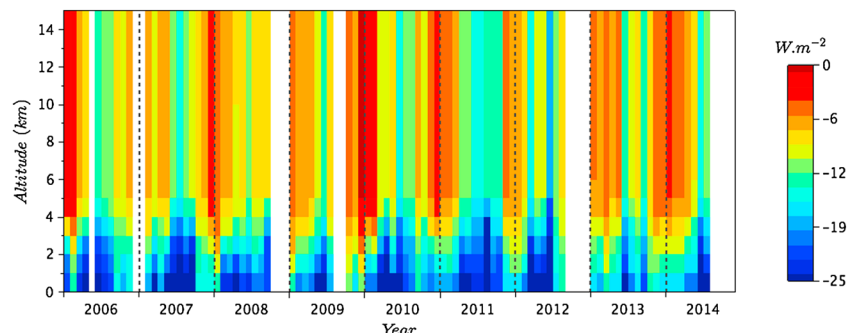


Figure 9. Monthly averages vertical profiles of direct aerosol net radiative effect between 2006 and 2014.

Table 3. Seasonal Solar Clear-Sky Direct Net Radiative Effect and Efficiency Integrated Over a Day^a

	Spring	Summer	Autumn	Winter
ΔF_{BOA} ($W m^{-2}$)	-24.47 (-0.21%)	-22.74 (-0.18%)	-17.25 (-0.00%)	-17.19 (-0.11%)
ΔF_{TOA} ($W m^{-2}$)	-8.31 (-3.35%)	-11.58 (-2.00%)	-8.33 (-2.69%)	-5.13 (-5.00%)
ΔF_{Atm} ($W m^{-2}$)	14.15 (+1.57%)	11.15 (1.52%)	8.92 (-2.36%)	12.06 (+1.85%)
ΔF_{BOA}^{eff} ($W m^{-2}$)	-51.14 (-0.42%)	-45.34 (-0.22%)	-52.13 (-0.00%)	-65.23 (-0.11%)
ΔF_{TOA}^{eff} ($W m^{-2}$)	-18.28 (-3.27%)	-23.49 (-2.35%)	-24.60 (-2.69%)	-18.68 (-4.56%)
ΔF_{Atm}^{eff} ($W m^{-2}$)	32.86 (+1.44%)	21.85 (+2.20%)	27.54 (+2.28%)	46.55 (+1.60%)

^aThe parentheses stand for the differences in retrieval when a standard Gaussian distribution is used for describing the aerosols vertical profile.

elevated layer simulated by a Gaussian distribution appears as better suited to summer and spring seasons, whereas a relatively higher concentration of aerosols is mainly observed at ground level during winter. In addition, this last season is associated with more absorbing particles. In presence of such aerosols, the estimation is more sensitive to their vertical distribution since they will interact differently, according to their altitude, with the radiation scattered by the molecules [Meloni et al., 2005]. However, despite relatively small differences that are observed at BOA and TOA, quite considerable differences (up to $10 W m^{-2}$) are found at the altitude of the aerosol layers if an assumed distribution is used instead of a real one. Uncertainties in ΔF and ΔF^{eff} are found as similar, as could be expected.

4.4. Heating Rates

The heating rates due to aerosol presence can be derived from the values of the calculated radiative effect (equation (7)). In Figure 11 we present the monthly averaged profiles for the contribution of aerosols and gases only as well as for the combination of these two.

The daily heating induced by the gases presents an annual cycle, maximum in summer and minimum in winter. This variation is explained by the combination of the change in concentration of gases (H_2O maximum during the wet season) and the sunshine duration (also maximum at this time). The heating rate induced by the molecules at ground level is thus about $0.64 K d^{-1}$ in summer and about $0.39 K d^{-1}$ in winter. At the ground level, the aerosols contribute, respectively, to 32%, 20%, 15%, and 38% of the total heating (gases and aerosols) from spring to winter. At an altitude of 3 km, their contribution is about 29%, 24%, 25%, and 28%, for absolute values of 0.25, 0.23, 0.19, and $0.17 W m^{-2}$.

5. Conclusions

Since 2003, a continuous aerosol monitoring is performed at the coastal Mbour observation platform located on a pathway of mineral dust and biomass burning aerosol from the Sahara desert and the Sahel. In their paper, Léon et al. [2009] presented the three first years of measurements performed on this site and suggested the need of extending the monitoring. Automatic procedures have been developed and implemented since that time in order to treat and interpret close to 10 years of Lidar and Sun photometer observations.

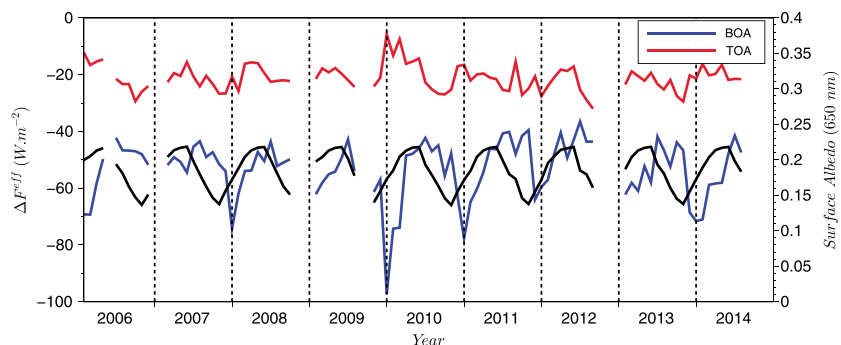


Figure 10. Solar clear-sky radiative effect efficiency at the top (in red) and the bottom (in blue) of the atmosphere. The black solid line is the surface albedo at 650 nm.

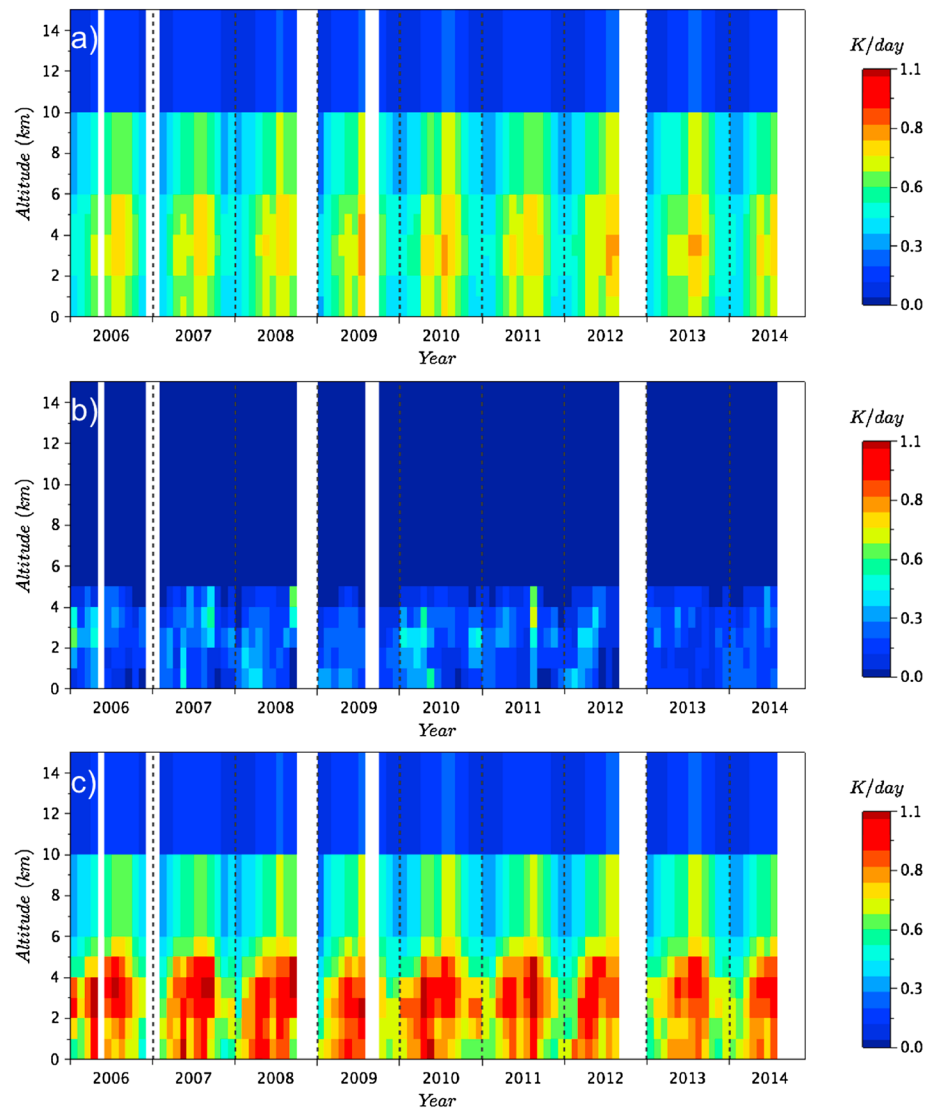


Figure 11. Solar clear-sky heating rates profiles (monthly averages) from 2006 to 2014 for the different atmospheric contributions: (a) gases, (b) aerosols, and (c) total.

The results presented in this work reveal some distinct patterns for the total column-integrated aerosol properties at different time scales that also imply different phenomena. Annual cycles are observed for each parameter with, as consequence, contrasted values for the different seasons. This contrast is maximum considering winter (dry season) and summer (wet season). Both these seasons are characterized by air masses of different origins. The influence of desert dust source regions is suggested by the back trajectories at ground level during winter and at higher altitude, in a thicker layer, during summertime, while the air masses close to the ground have been transported over the Atlantic Ocean. The resulting variation in the nature of the particles gives contrasted seasonal aerosol properties. The summer is thus characterized by a high aerosol load ($AOT=0.57$) composed of large ($\alpha=0.23$) and weakly absorbing ($\omega_0=0.94$) particles (mainly dust). In contrast, finer absorbing particles ($\alpha=0.48$ and $\omega_0=0.87$) are observed during winter and are associated with a lower aerosol burden ($AOT=0.32$). The high absorption is explained by the sporadic transport of biomass burning particles during autumn and winter, but mostly by the local emissions from wood-fired ovens or from the transport whose proportion (regarding to dust) is higher in winter and autumn. This local influence explains the weekly trends observed (AOT variation about 7%) and contributes to the daily trends due to the meteorological conditions reported here (relative humidity and wind speed). The long-term set of observations, analyzed through application of the seasonal Mann-Kendall test, reveals a significant decrease

of AOT about 30% during autumn. The Lidar ratio derived from the combined Lidar and Sun photometer inversion differs from the AERONET derived one. The average is about 40 ± 15 sr and tends to increase with α even though no neat seasonal cycle can be observed. The vertical distribution of the aerosols is complex over this site since the desert dust is transported in an elevated layer in spring and summer and close to the ground during winter. This transport is clearly visible from the derived extinction profiles that show, beyond the interannual variability, quite reproducible seasonal patterns ($\sigma_{\text{ext}} = 0.04 \text{ km}^{-1}$ in winter and $\sigma_{\text{ext}} = 0.09 \text{ km}^{-1}$ in summer at a height of 3 km).

An accurate estimation of the clear-sky shortwave direct radiative effect has been performed using combination of Sun photometer and Lidar retrievals. A differential study highlighted the importance of the aerosol vertical distribution knowledge. Usage of a standard Gaussian profile assumption can result in large differences ($>10 \text{ W m}^{-2}$) at the altitude of aerosol layers. The differences found for this site at the TOA and BOA are, however, significantly lower. At the same time, uncertainties at TOA and BOA present a pronounced annual dependence. That is, the differences at TOA are of about 2% in summer and about 5% in winter. The aerosol radiative effect values themselves also present seasonality. From spring to winter, daily average values of 14.15 W m^{-2} , 11.15 W m^{-2} , 8.92 W m^{-2} , and 12.06 W m^{-2} have been calculated for the clear-sky atmospheric radiative effect. The aerosols are characterized by a higher radiative efficiency during winter (46.55 W m^{-2}) than during summer (32.86 W m^{-2}). The derivation of the aerosol solar clear-sky heating rate reveals that the particles can contribute up to 38% of the total atmospheric heating in the wintertime.

Continuous aerosol observations and real-time data processing are maintained in the Mbour site up to the present. The interest of such observations is reinforced when studying short-time phenomenon and for getting unbiased averages, especially when daily cycles exist. In their work, Kaufman *et al.* [2000] present a comparison of aerosol observations (AOT and α) between AERONET and Terra/Aqua satellites observations that are performed over 90 min time window per day. The time window restriction involves a weak difference (about 2%) for the global averaged AOT. The computation of the seasonal averages over Mbour performed, on one hand, with all the day measurements and, on the other hand, with measurements corresponding to the Terra track, reveals greater differences. These ones can be explained by the daily cycles described previously. Thus, by limiting AERONET observations to Terra observation conditions, the averaged AOT would be 2% higher in summer and 6% lower in winter. The difference reaches +17% regarding α in the wintertime.

The continuity of the observations performed over this station for several years makes the Mbour site as particularly interesting for comparison exercises with output models [Cuevas *et al.*, 2015] or satellites. These continuous observations can be punctually reinforced through intensive field campaigns. Thus, in March 2015 was started a multidisciplinary Study of SaHaran Dust Over West Africa 2 campaign thanks to the cooperation of seven French laboratories involved in the Chemical and Physical Properties of the Atmosphere labex project. Additional measurements are performed and complement the existing observations. A powerful multiwavelength Lidar (LILAS) is providing vertical profiles at several wavelengths with Raman and depolarization information. These profiles, which do not require any vertical homogeneity assumption, could be used for evaluating the extinction profiles derived from the simple monowavelength Lidar used in this work. The validation of the profiles could be investigated as well with the mobile Sun photometer Photomètre Léger Aéroporté pour la Surveillance des Masses d'Air (PLASMA) [Karol *et al.*, 2012], which performs airborne measurements and provides optical thickness profiles at several wavelengths. A commonly recognized weakness of most of the Lidars, which is in the accuracy of the measurements at low altitude, was also addressed in this field campaign by performing ground-based nephelometer measurements aiming examination of the lowest layers homogeneity hypothesis.

Acknowledgments

We are very grateful to the scientific and technical staff of the IRD and of the Service d'Observation PHOTONS/AERONET (INSU/CNRS). The back trajectories have been computed thanks to NOAA HYSPLIT Air Resource Laboratory model (<http://ready.arl.noaa.gov/HYSPLIT.php>). The research leading to these results has received, through ACTRIS, funding from the European Union Seventh Framework Program (FP7/2007–2013) under grant agreement 262254.

References

- Ansmann, A., H. Baars, and M. Tesche (2009), Dust and smoke transport from Africa to South America: Lidar profiling over Cape Verde and the Amazon rainforest, *Geophys. Res. Lett.*, *36*, L11802, doi:10.1029/2009GL037923.
- Baars, H., A. Ansmann, R. Engelmann, and D. Althausen (2008), Continuous monitoring of the boundary-layer top with lidar, *Atmos. Chem. Phys.*, *8*(23), 7281–7296, doi:10.5194/acp-8-7281-2008.
- Bäumer, D., R. Rinke, and B. Vogel (2008), Weekly periodicities of aerosol optical thickness over central Europe—Evidence of an anthropogenic direct aerosol effect, *Atmos. Chem. Phys.*, *8*(1), 83–90, doi:10.5194/acp-8-83-2008.
- Bergametti, G., L. Gomes, G. Gausson, P. Rognon, and M. Coustumer (1989), African dust observed over Canary Islands: Source regions identification and transport pattern for some summer situations, *J. Geophys. Res.*, *94*(D12), 14,855–14,864, doi:10.1029/JD094iD12p14855.

- Brooks, I. M. (2003), Finding boundary layer top: Application of a wavelet covariance transform to lidar backscatter profiles, *J. Atmos. Oceanic Technol.*, *20*, 1092–1105, doi:10.1175/1520-0426(2003)020<1092:FBLTAO>2.0.CO;2.
- Cattrell, C., J. Reagan, K. Thome, and O. Dubovik (2005), Variability of aerosol and spectral lidar and backscatter and extinction ratios of key aerosol types derived from selected Aerosol Robotic Network locations, *J. Geophys. Res.*, *110*(D10), doi:10.1029/2004JD005124.
- Cavalieri, O., et al. (2010), Variability of aerosol vertical distribution in the Sahel, *Atmos. Chem. Phys.*, *10*(24), 12,005–12,023, doi:10.5194/acp-10-12005-2010.
- Chew, B. N., J. R. Campbell, J. S. Reid, D. M. Giles, S. V. Salinas, and S. C. Liew (2010), Optically thin cirrus cloud contamination in sun photometer data. [Available at <http://scholarbank.nus.edu.sg/handle/10635/115466>.]
- Chiapello, I., G. Bergametti, and L. Gomes (1995), An additional low layer transport of Sahelian and Saharan dust over the north-eastern tropical Atlantic, *Geophys. Res. Lett.*, *22*, 3191–3194, doi:10.1029/95GL03313.
- Chiapello, I., G. Bergametti, and B. Chatenet (1997), Origins of African dust transported over the northeastern tropical Atlantic, *J. Geophys. Res.*, *102*(D12), 13,701–13,709, doi:10.1029/97JD00259.
- Cuevas, E., et al. (2015), The MACC-II 2007–2008 reanalysis: Atmospheric dust evaluation and characterization over northern Africa and the Middle East, *Atmos. Chem. Phys.*, *15*, 3991–4024.
- Deboudt, K., P. Flament, M. Choël, and A. Gloter (2010), Mixing state of aerosols and direct observation of carbonaceous and marine coatings on African dust by individual particle analysis, *J. Geophys. Res.*, *115*, D24207, doi:10.1029/2010JD013921.
- Delmas, R. A., P. Loudjani, and A. Podaire (1991), Biomass burning in Africa: An assessment of annually burned biomass, in *Global Biomass Burning: Atmospheric, Climatic, and Biospheric Implications*, pp. 126–132, MIT Press, Cambridge, Mass. [Available at https://inis.iaea.org/search/search.aspx?orig_q=RN:23066755.]
- Derimian, Y., J. - F. Léon, O. Dubovik, I. Chiapello, D. Tanré, A. Sinyuk, F. Auriol, T. Podvin, G. Brogniez, and B. Holben (2008a), Radiative properties of aerosol mixture observed during the dry season 2006 over M'Bour, Senegal (African Monsoon Multidisciplinary Analysis campaign), *J. Geophys. Res.*, *113*, D00C09, doi:10.1029/2008JD009904.
- Derimian, Y., A. Karnieli, Y. Kaufman, M. Andreae, T. Andreae, O. Dubovik, W. Maenhaut, and I. Koren (2008b), The role of iron and black carbon in aerosol light absorption, *Atmos. Chem. Phys.*, *8*(13), 3623–3637, doi:10.5194/acp-8-3623-2008.
- Derimian, Y., O. Dubovik, D. Tanre, P. Goloub, T. Lapyonok, and A. Mortier (2012), Optical properties and radiative forcing of the Eyjafjallajökull volcanic ash layer observed over Lille, France, in 2010, *J. Geophys. Res.*, *117*, D00U25, doi:10.1029/2011JD016815.
- Dubovik, O., and M. King (2000), A flexible inversion algorithm for retrieval of aerosol optical properties from Sun and sky radiance measurements, *J. Geophys. Res.*, *105*(D16), 20,673–20,696, doi:10.1029/2000JD900282.
- Dubovik, O., A. Smirnov, B. Holben, M. King, Y. Kaufman, T. Eck, and I. Slutsker (2000), Accuracy assessments of aerosol optical properties retrieved from Aerosol Robotic Network (AERONET) Sun and sky radiance measurements, *J. Geophys. Res.*, *105*(D8), 9791–9806, doi:10.1029/2000JD900040.
- Dubovik, O., B. Holben, T. Lapyonok, A. Sinyuk, M. Mishchenko, P. Yang, and I. Slutsker (2002), Non-spherical aerosol retrieval method employing light scattering by spheroids, *Geophys. Res. Lett.*, *29*(10), 1415, doi:10.1029/2001GL014506.
- Dubuisson, P., J. C. Buriez, and Y. Fouquart (1996), High spectral resolution solar radiative transfer in absorbing and scattering media: Application to the satellite simulation, *J. Quant. Spectros. Radiat. Transfer*, *55*(1), 103–126.
- Dubuisson, P., J. C. Roger, M. Mallet, and O. Dubovik (2006), A code to compute the direct solar radiative forcing: Application to anthropogenic aerosols during the Escompte experiment, *Curr. Probl. Atmos. Radiat.*, 127–130.
- Esselborn, M., M. Wirth, A. Fix, B. Weinzierl, K. Rasp, M. Tesche, and A. Petzold (2009), Spatial distribution and optical properties of Saharan dust observed by airborne high spectral resolution lidar during SAMUM 2006, *Tellus, Ser. B*, *61*(1), 131–143, doi:10.1111/j.1600-0889.2008.00394.x.
- Flament, P., K. Deboudt, H. Cachier, B. Châtenet, and X. Mériaux (2011), Mineral dust and carbonaceous aerosols in West Africa: Source assessment and characterization, *Atmos. Environ.*, *45*(22), 3742–3749, doi:10.1016/j.atmosenv.2011.04.013.
- Gama, C., O. Tchepel, J. Baldasano, S. Basart, J. Ferreira, C. Pio, J. Cardoso, and C. Borrego (2015), Seasonal patterns of Saharan dust over Cape Verde—A combined approach using observations and modelling, *Tellus, Ser. B*, *67*, 1–21, doi:10.3402/tellusb.v67.24410.
- García, O. E., A. M. Diaz, and F. J. Exposito (2008), Validation of AERONET estimates of atmospheric solar fluxes and aerosol radiative forcing by ground-based broadband measurements, *J. Geophys. Res.*, *113*, D21207, doi:10.1029/2008JD010211.
- García, O., J. Díaz, F. Exposito, A. Díaz, O. Dubovik, Y. Derimian, P. Dubuisson, and J.-C. Roger (2012), Shortwave radiative forcing and efficiency of key aerosol types using AERONET data, *Atmos. Chem. Phys.*, *12*(11), 5129–5145, doi:10.5194/acp-12-5129-2012.
- Gassó, S., et al. (2003), Influence of humidity on the aerosol scattering coefficient and its effect on the upwelling radiance during ACE-2, *Tellus, Ser. B*, *52*(2), 546–567, doi:10.1034/j.1600-0889.2000.00055.x.
- González, R. S., and A. J. Urós (2011), Transport of desert dust mixed with North African industrial pollutants in the subtropical Saharan Air Layer. [Available at <http://rabida.uhu.es/dspace/handle/10272/6052>.]
- Guan, H., B. Schmid, and A. Bucholtz (2010), Sensitivity of shortwave radiative flux density, forcing, and heating rate to the aerosol vertical profile, *J. Geophys. Res.*, *115*, D06209, doi:10.1029/2009JD012907.
- Gyoswami, B. N., and J. Shukla (1984), Quasi-periodic oscillations in a symmetric general circulation model, *J. Atmos. Sci.*, *41*(1), 20–37, doi:10.1175/1520-0469(1984)041<0020:QPOIAS>2.0.CO;2.
- Haywood, J. M., J. Pelon, P. Formenti, N. Bharmal, M. Brooks, G. Capes, P. Chazette, C. Chou, S. Christopher, and H. Coe (2008), Overview of the dust and biomass burning experiment and African monsoon multidisciplinary analysis special observing period 0, *J. Geophys. Res.*, *113*, D00C17, doi:10.1029/2008JD010077.
- Haywood, J., and O. Boucher (2000), Estimates of the direct and indirect radiative forcing due to tropospheric aerosols: A review, *Rev. Geophys.*, *38*(4), 513–543, doi:10.1029/1999RG000078.
- Haywood, J., P. Francis, and S. Osborne (2003), Radiative properties and direct radiative effect of Saharan dust measured by the C-130 aircraft during SHADE: 1. Solar spectrum, *J. Geophys. Res.*, *108*(D18), 8577, doi:10.1029/2002JD002687.
- Heintzenberg, J. (2009), The SAMUM-1 experiment over Southern Morocco: Overview and introduction, *Tellus, Ser. B*, doi:10.1111/j.1600-0889.2008.00403.x.
- Holben, B. N., et al. (1998), AERONET—A federated instrument network and data archive for aerosol characterization, *Remote Sens. Environ.*, *66*, 1–16, doi:10.1016/S0034-4257(98)00031-5.
- Jin, M., J. Shepherd, and M. King (2005), Urban aerosols and their variations with clouds and rainfall: A case study for New York and Houston, *J. Geophys. Res.*, *110*, D10S20, doi:10.1029/2004JD005081.
- Kandler, K., N. Benker, U. Bundke, and E. Cuevas (2007), Chemical composition and complex refractive index of Saharan Mineral Dust at Izana, Tenerife (Spain) derived by electron microscopy, *Atmos. Environ.*, *41*(37), 8058–8074, doi:10.1016/j.atmosenv.2007.06.047.

- Karol, Y., D. Tanré, P. Goloub, C. Ververaerde, J. Y. Balois, L. Blarel, T. Podvin, A. Mortier, and A. Chaikovskiy (2012), Airborne Sunphotometer PLASMA: Concept, measurements, comparison of aerosol extinction vertical profile with lidar, *Atmos. Meas. Tech. Discuss.*, 5(5), 6813–6834.
- Kaufman, Y. J., B. N. Holben, D. Tanré, I. Slutsker, T. Eck, and A. Smirnov (2000), Will aerosol measurements from the Terra polar orbiting satellite represent the daily aerosol abundance and properties, *Geophys. Res. Lett.*, 27, 3861–3864, doi:10.1029/2000GL011968.
- Klett, J. (1981), Stable analytical inversion solution for processing lidar returns, *Appl. Opt.*, 20(2), 211–220, doi:10.1364/AO.20.000211.
- Klett, J. (1985), Lidar inversion with variable backscatter/extinction ratios, *Appl. Opt.*, 24(11), 1638–1643, doi:10.1364/AO.24.001638.
- Léon, J.-F., Y. Derimian, I. Chiapello, D. Tanré, T. Podvin, B. Chatenet, A. Diallo, and C. Deroo (2009), Aerosol vertical distribution and optical properties over M'Bour (16.96°W; 14.39°N), Senegal from 2006 to 2008, *Atmos. Chem. Phys.*, 9(23), 9249–9261, doi:10.5194/acp-9-9249-2009.
- Liousse, C., et al. (2010), Updated African biomass burning emission inventories in the framework of the AMMA-IDAF program, with an evaluation of combustion aerosols, *Atmos. Chem. Phys.*, 10(19), 9631–9646, doi:10.5194/acp-10-9631-2010.
- Marr, L. C., and R. A. Harley (2002), Spectral analysis of weekday-weekend differences in ambient ozone, nitrogen oxide, and non-methane hydrocarbon time series in California, *Atmos. Environ.*, 36(14), 2327–2335, doi:10.1016/S1352-2310(02)00188-7.
- Marticoirena, B., B. Chatenet, J. Rajot, S. Traoré, M. Coulibaly, A. Diallo, I. Koné, A. Maman, T. NDiaye, and A. Zakou (2010), Temporal variability of mineral dust concentrations over West Africa: Analyses of a pluriannual monitoring from the AMMA Sahelian Dust Transect, *Atmos. Chem. Phys.*, 10(18), 8899–8915, doi:10.5194/acp-10-8899-2010.
- Meloni, D., A. Sarra, T. Iorio, and G. Fiocco (2005), Influence of the vertical profile of Saharan dust on the visible direct radiative forcing, *J. Quant. Spectros. Radiat. Transfer*, 93(4), 397–413, doi:10.1016/j.jqsrt.2004.08.035.
- Mortier, A. (2013), Tendances et variabilités de l'aérosol atmosphérique à l'aide du couplage Lidar/Photomètre sur les sites de Lille et Dakar thèse de doctorat, Optique et laser, Physico-chimie, Atmosphère, French.
- Müller, D., A. Ansmann, I. Mattis, M. Tesche, U. Wandinger, D. Althausen, and G. Pisani (2007), Aerosol-type-dependent lidar ratios observed with Raman lidar, *J. Geophys. Res.*, 112(D16), doi:10.1029/2006JD008292.
- Osborne, S., B. Johnson, J. Haywood, A. Baran, M. Harrison, and C. McConnell (2008), Physical and optical properties of mineral dust aerosol during the dust and biomass-burning experiment, *J. Geophys. Res.*, 113, D00C03, doi:10.1029/2007JD009551.
- Pal, S. R., W. Steinbrecht, and A. I. Carswell (1992), Automated method for lidar determination of cloud-base height and vertical extent, *Appl. Opt.*, 31(10), 1488–1494.
- Papayannis, A., et al. (2008), Systematic lidar observations of Saharan dust over Europe in the frame of EARLINET (2000–2002), *J. Geophys. Res.*, 113, D10204, doi:10.1029/2007JD009028.
- Pelon, J., M. Mallet, A. Mariscal, P. Goloub, D. Tanré, D. Karam, C. Flamant, J. Haywood, B. Pospichal, and S. Victori (2008), Microlidar observations of biomass burning aerosol over Djougou (Benin) during African Monsoon Multidisciplinary Analysis Special Observation Period 0: Dust and Biomass-Burning Experiment, *J. Geophys. Res.*, 113, D00C18, doi:10.1029/2008JD009976.
- Powell, D., J. Reagan, M. Rubio, W. Erxleben, and J. Spinhirne (2000), ACE-2 multiple angle micro-pulse lidar observations from Las Galletas, Tenerife, Canary Islands, *Tellus, Ser. B*, 52(2), 652–661, doi:10.1034/j.1600-0889.2000.00059.x.
- Prospero, J. M., P. Ginoux, and O. Torres (2002), Environmental characterization of global sources of atmospheric soil dust identified with the Nimbus 7 Total Ozone Mapping Spectrometer (TOMS) absorbing aerosol product, *Rev. Geophys.*, 40(1), 1002, doi:10.1029/2000RG000095.
- Roger, J. C., M. Mallet, P. Dubuisson, H. Cachier, E. Vermote, O. Dubovik, and S. Despiou (2006), A synergetic approach for estimating the local direct aerosol forcing: Application to an urban zone during the Expérience sur Site pour Contraindre les Modèles de Pollution et de Transport d'Emission (ESCOMPTE) experiment, *J. Geophys. Res.*, 111, D13208, doi:10.1029/2005JD006361.
- Satheesh, S., and K. Krishnamoorthy (2005), Radiative effects of natural aerosols: A review, *Atmos. Environ.*, 39(11), 2089–2110, doi:10.1016/j.atmosenv.2004.12.029.
- Schuster, G. L., O. Dubovik, and B. N. Holben (2006), Angstrom exponent and bimodal aerosol size distributions, *J. Geophys. Res.*, 111, D07207, doi:10.1029/2005JD006328.
- Seidel, D., C. Ao, and K. Li (2010), Estimating climatological planetary boundary layer heights from radiosonde observations: Comparison of methods and uncertainty analysis, *J. Geophys. Res.*, 115, D16113, doi:10.1029/2009JD013680.
- Smirnov, A., B. N. Holben, T. F. Eck, O. Dubovik, and I. Slutsker (2000), Cloud-screening and quality control algorithms for the AERONET database, *Remote Sens. Environ.*, 73(3), 337–349, doi:10.1016/S0034-4257(00)00109-7.
- Smirnov, A., B. Holben, T. Eck, I. Slutsker, B. Chatenet, and R. Pinker (2002), Diurnal variability of aerosol optical depth observed at AERONET (Aerosol Robotic Network) sites, *Geophys. Res. Lett.*, 29(23), 2115, doi:10.1029/2002GL016305.
- Tanré, D., J. Haywood, J. Pelon, and J. F. Léon (2003), Measurement and modeling of the Saharan dust radiative impact: Overview of the Saharan Dust Experiment (SHADE), *J. Geophys. Res.*, 108(D18), 8574, doi:10.1029/2002JD003273.
- Viana, M., X. Querol, A. Alastuey, and E. Cuevas (2002), Influence of African dust on the levels of atmospheric particulates in the Canary Islands air quality network, *Atmos. Environ.*, 36(38), 5861–5875, doi:10.1016/S1352-2310(02)00463-6.
- Voss, K., E. Welton, P. Quinn, J. Johnson, A. Thompson, and H. Gordon (2001), Lidar measurements during Aerosols99, *J. Geophys. Res.*, 106(D18), 20,821–20,831, doi:10.1029/2001JD900217.
- Welton, E. J., K. J. Voss, H. R. Gordon, and H. Maring (2000), Ground-based lidar measurements of aerosols during ACE-2: Instrument description, results, and comparisons with other ground-based and airborne measurements, *Tellus, Ser. B*, 52, 636–651, doi:10.1034/j.1600-0889.2000.00025.x.